Modelling of the static and dynamic mechanical properties of human otoliths

DISSERTATION

zur Erlangung des Grades eines Doktors
der Naturwissenschaften
der Fakultät für Mathematik und Physik
der Eberhard-Karls-Universität zu Tübingen

vorgelegt von

Rudolf Jäger

aus Ellwangen

2003

Fluctuat nec mergitur
Motto of the city of Paris

Abstract

The aim of this study is a numerical investigation of the static and dynamic properties of the otoliths. The otoliths are a part of the vestibular system, located in the inner ears. They sense accelerations of the head. In the static case, information retrieved from them indicates the orientation of the head with respect to gravity. Under dynamic conditions, they provide information about the current direction and magnitude of head acceleration. Two important parts of the otoliths can be distinguished with respect to their function in the sensory apparatus, the otolith membrane and macula. The otolith membrane, a flat, layered filament structure is deformed by head accelerations. Though materials within the inner ear have similar densities, this membrane is subject to external accelerations because it contains higher density crystals, known as otoconia. The otolith macula contains hair cells, the sensory units of the otoliths. These cells feature small hair bundles which protrude into the otolith membrane, superimposed on the macula. If the membrane is deformed, the hair bundles are tilted and associated hair cells change their polarization. The resulting signal is subsequently reported to the brain.

Up to now little work has been devoted to this sensory apparatus though it is known that it plays a important role within the vestibular system. The current investigation tries to improve the understanding of this structure by simulating the responses of the otolith membrane, using the method of finite elements (FEM). This method is especially well suited for this problem since the curved boundary and shape of the otolith membrane present no problem to it. As a result of this approach, membrane displacements are obtained which depend on the direction and magnitude of head acceleration.

Based on recent findings with regard to the morphology of the membrane and measurements of the 3 dimensional (3D) shape of the otolith macula, the numerical model tries to mimic information processing by these sensors as close as possible. Deformations of the membrane depend on the local orientation of the macula and the direction of head acceleration. The model suggests that interactions within the membrane are of minor importance. This means that different parts of the membrane with different orientation interact weakly. The curved shape of the macula only affects interactions in small membrane areas, which have high local curvature. To verify FEM results, the dynamics of the membrane were studied using transfer functions. We derived the functions for the case of an infinitely extended, planar membrane. Comparison with corresponding FEM results showed only minor discrepancies. From this it may be concluded that the lateral border of the otolith

membrane has no effect on the movement of the whole structure and only leads to appreciable effects in the vicinity of the border. Our results also predict that otoconia may exhibit resonant behavior within their supporting filament matrix. This resonance is expected to occur for frequencies between 100 and 1000 Hz. If such a resonance exists, structural damage can be imposed on the otolith membrane by loud sounds from the frequency range mentioned above.

The polarization is determined by the tilt of hair bundles associated with the cells. Based on the local displacement of the otolith membrane, the polarization of hair cells was calculated. This modelling indicates that head orientation with respect to gravity as well as time-dependent changes of head acceleration are represented in a distributed fashion on the macula level.

Contents

List of Figures

List of Tables

1 Introduction

1.1 The Vestibular System

The essential task of the vestibular system is to gather information about body posture and movement which allows us to maintain balance while standing upright and move through space. It is also of great importance for the visual system since focusing on a specific target during movements requires knowledge about head position and velocity. These skills are thought to be essential for surviving. Several sensory systems are involved in gathering this kind of information. Movements of the head are primarily sensed by the vestibular organs which are located in the inner ears. Further cues about the body state of position and motion are deduced from visual information. Proprioceptive receptors located in muscles and tactile sensors under the skin of hands and feet are also involved in this task. There is further evidence that vestibular information is gathered from receptors probably located in the kidneys or liver (Mittelstaedt, 1995). All this sensory information is integrated in the brain to form a consistent representation of body posture and movement. The vestibular system thereby plays a dominant role, especially for eye movements. Impairments of this system can result in severe disorientation and nausea.

Of all the sensors participating in the vestibular system, the vestibular organ has acquired special attention. This is mainly due to our spatial orientation, which is predominantly guided by sensory inputs originating in this organ. Eye movements are fairly simple to measure and a direct link exists between vestibular input and ocular output. Since visual cues are eminently important in everyday life, disorders of the vestibular-ocular system and their treatment are of great medical interest. Because of this, an understanding of this system and the way of information processing performed by it, is highly valuable.

The human vestibular organ is made up of two distinct subsystems: the *semicircular canals* and the *otoliths*. While the semicircular canals (see Fig. 1) measure head angular velocity, the otoliths provide magnitude and direction of head acceleration. Those accelerations can either be related to changes of head velocity or gravity. The term otolith will refer here to all structural and functional aspects of this organ. Sensory inputs from the semicircular canals and the otoliths need to be combined to form a consistent picture of the state of head movement. This process is called sensory integration and examples of it can be found in many other biological sensory systems. There is also a wide range of technical applications where sensory integrations needs to be performed. Thus sensory integration represents a general problem and it is interesting to understand how nature solves it. The vestibular organ is particularly suited to study this process since it is build relatively simple compared with other human sensory systems. Facilities exist further to apply a wide

range of vestibular stimuli accompanied with simultaneous measurement of ocular movements.
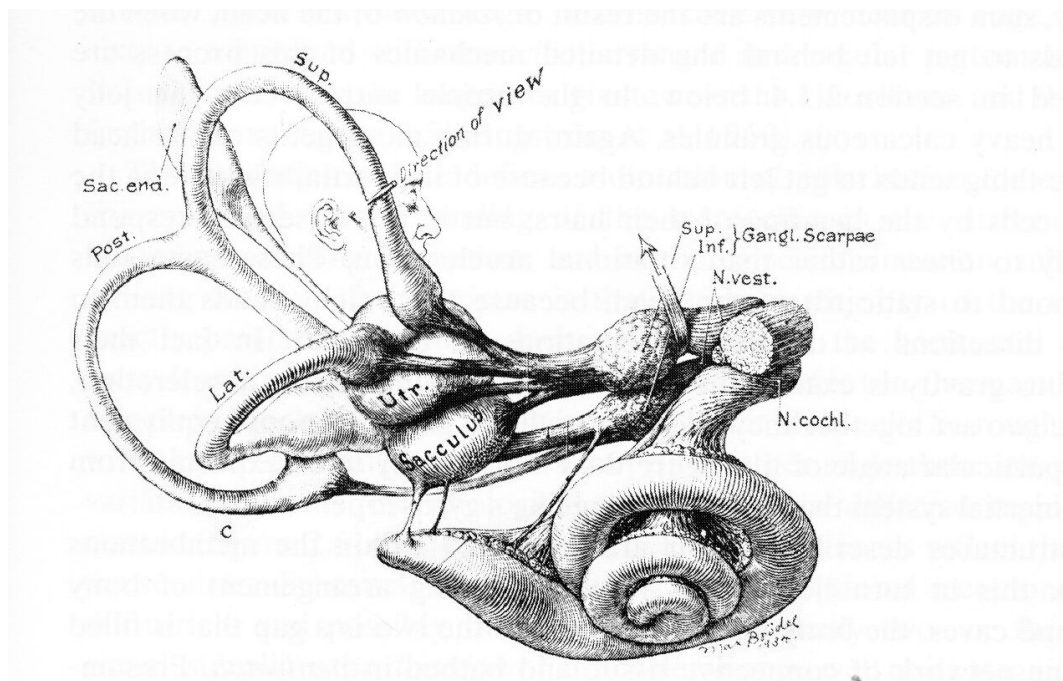
Figure 1: The inner ear labyrinth and its orientation with respect to the head. The arc-like structures on the left are the three semicircular canals, while the sacs which host the otoliths are visible in the center. The spiral structure on the lower right is the cochlea, the sensory organ of hearing. All this organs are innervated by neurons that belong to the vestibular nerve. The figure is due to Max Brodel (1937).

The interest in the vestibular organ and specifically the otoliths is further increased by the observation that space motion sickness is likely related to them (Diamond and Markham, 1992; Markham et al., 2000). This nauseatic state, induced by movements in a zero g environment, is known since the start of human spaceflight. About 60% of all humans send to space are susceptible to this more or less severe distortion. Adaptation to the new environment happens after several days. During everyday life the brain is used to certain combinations of inputs from different sensors and has representations for them. If sensory integration leads to a state which cannot be resolved within this usual patters, nausea is a common reaction of the body. For example many people feel sick while reading on a bus. In this case the eye movements for reading do not correspond with the vestibular signals, induced by the movements of the bus. There are reasons to believe that this effect, termed sensory mismatch, also causes space motion sickness, though the exact path which leads to this phenomenon is unknown.

Progress to the solution of these problems requires a close understanding of how external stimuli are transformed to neural signals by the sensory systems.

Any movement in space is composed of a rotatory and a translatory component, and the vestibular organ has accordingly evolved ways to transduce these two types of stimuli: the semicircular canals, which respond to rotatory movements, and the otoliths (also known as maculae organs), which indicate translatory movements and gravity. Our understanding of these structures is largely based on two pillars: on the one side, an extensive experimental database exists about eye movements elicited by linear or rotational movements of the head in space. The large interest in this type of investigation is in part based on the significant clinical applications, which allow important diagnostic conclusions from the observed eye movements. The other focus of investigations has been on the study of structure and function of individual hair cells. They are the mechanical sensors of the inner ear, found in the otoliths, semicircular canals and the auditory system. On this front, one of the driving forces is the importance of hair cells for the understanding of hearing function and deficits. The structure connecting these two pillars, i.e. the transduction of actual head movements into displacements of individual hair cells, is less well understood. In particular, research in this area has concentrated on the transduction properties of the semicircular canals (Rabbitt et al., 1995). Investigations have obtained considerable knowledge about the mechanical displacement at the sensory hair-cells, and a close understanding of these displacements, even for high accelerations and with plugged semicircular canals (Damiano and Rabbitt, 1996; Rabbitt et al., 1999). We further have a detailed knowledge about the anatomical connections that transduce these stimuli (Leigh and Zee, 1999). In contrast, determining the appropriate response to a head acceleration, which is mediated by the otoliths, is computationally and behaviorally much more complex. First of all, the central nervous system (CNS) is confronted with an ambiguous stimulus: the forces acting on the otoliths may be coming from a change in the orientation with respect to gravity (e.g. a head tilt to the left), or they may be due to accelerations (e.g. a acceleration to the right). Once the CNS has established its best guess about the direction and magnitude of the acceleration, it has to consider the fixation distance in establishing the appropriate response, i.e. the eye movement response that will keep the target of interest on the fovea: keeping our eyes on a target 10 cm in front of our face while moving the head left or right requires large compensatory eye movements; looking at the moon during the same movement requires practically no eye movements.

One way to determine the way accelerations are transformed to neural signals is the use of a numerical model that takes into account all known facts about the otoliths. A numerical model also allows to investigate the effect of three-dimensional (3D) orientation and shape of the otolith maculae, the sensory organs of the otoliths (also known as sensory epithelium). Several anatomical investigations have focused on
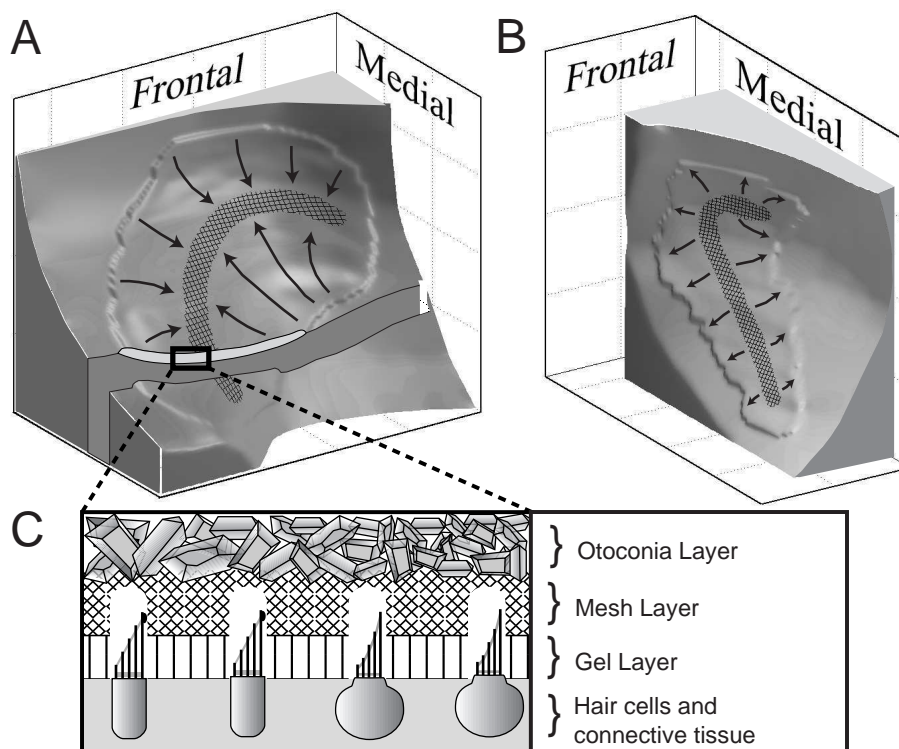
Figure 2: Shape of left Utricle (A) and Saccule (B). A section of the layered otolith structure is shown in (C) indicating the otoconia-, mesh- and gel-layer. The shaded regions in the center of the otoliths has special properties and is termed striola. Arrows indicate the direction of hair cell polarizations.

this issue (Takagi and Sando, 1988; Sato et al., 1992; Curthoys et al., 1999).

The otoliths, utricle and saccule are basically flat (2-dimensional) structures located in the inner ear labyrinth (Fig. 1). Both can be identified by the shape of their lateral boundaries: While the saccule resembles an inverted L, the utricle has a more compact kidney-like shape. Contrary to long-standing assumptions they are not planar but show some substantial curvature (Takagi and Sando, 1988; Curthoys et al., 1999). Otoliths are organized structurally in several layers with mechanically different properties (Fig. 2). One of their most remarkable features, also indicated in the word "oto-lith" (ear-stone), are crystals embedded in the topmost layer. The density of these crystals is higher than the surrounding materials and accelerations of the head result in forces acting on them. The underlying mesh and gel layer can be distinguished by the different structure of their filament matrix. Like the otoconia layer, they are part of the *otolith membrane.* The term otolith membrane

is used for all filament parts of the otolith system that are displaced with respect to the head. The layers are superimposed on the sensory organ of the otoliths, known as macula, which is made of hair cells and connective tissue. Hair cells "sense" displacements via hair bundles attached to them. Bending of the bundles results in de- or hyperpolarization of the corresponding hair cell. The bending direction which leads to maximum excitation of the cell is termed polarization direction and may be characterized with a vector.

Up to now, the prevailing view, published in many textbooks, was that otoliths are planar structures aligned with the head coordinate system (see Fig. 3). It was assumed that the utricle lies in a horizontal and the saccule in a vertical plane, thus resulting in an angle of 90° between them. In accordance with these assumptions, figure 3 shows deformations of the otolith membrane in head upright position for two acceleration cases. Figure 3A shows shear displacements in the sacculus, which are caused by gravity. Additional acceleration to the left leads to displacements of the utricle in figure 3B.
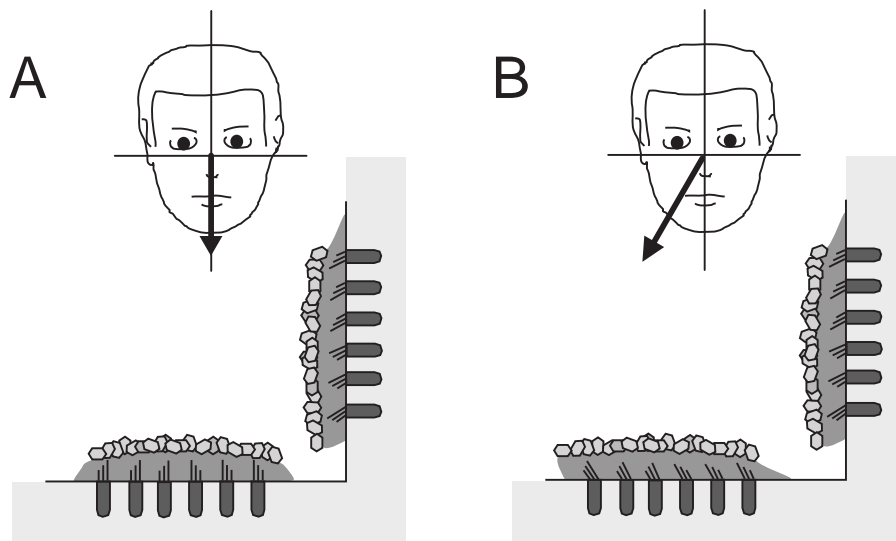
Figure 3: Simplified view of utricular and saccular otolith shapes in head upright position. The sections of the otoliths reveal shear displacements of the sacculus in the case of gravitational forces alone (A) and additional displacements of the utricle for an acceleration to the left (B).

Though this view captures the qualitative properties of otolith mechanics, any quantitative investigation of this system needs to address the curved shape of these structures. In this study finite element analysis was employed to incorporate the curvature of the maculae into a model of the otolith membrane. Using this well-known technique, the equilibrium and dynamic displacements of the otolith membrane were

calculated. One of the central questions regarding displacements is to what degree the curvature affects movements of the membrane as a whole. If the mechanical coupling within the membrane were strong enough, displacement of one part of the membrane would lead to displacements of other parts as well. Observations have shown that accelerations that are locally perpendicular to the membrane do not lead to displacements. Due to the curvature it would theoretically be possible though that even parts that are locally perpendicular to the acceleration get displaced by forces transmitted through the otolith membrane. Even the nature of displacements elicited by simple static accelerations in various directions is not yet known. It would be easy to think of a mechanical system where the curvature of a surface allows movements in one direction but prevents displacements in others. Does such an effect happen in the otolith system?

Based on the calculated membrane displacements and the measured directions of hair cell polarization it is possible to determine the distribution of hair cell excitation on the whole otolith macula (Kondrachuk and Sirenko, 1987). It is expected that accelerations in different directions lead to corresponding, different excitation patterns. What do these patterns look like? What are the typical distances on the macula were changes in the patterns arise? It is also interesting to compare the findings of numerical models with the results of experimental investigations of otolith signals in the vestibular nerve (Fernandez and Goldberg, 1976a,b; Goldberg et al., 1990a). Recordings from the vestibular nerve using exactly the same paradigm as employed in our numerical investigation (Fernandez et al., 1972) have found a remarkably rich set of single-neuron discharge rates. To test the results of our numerical model, we compared our theoretical results with these experimental findings.

1.2 The Otolith Membrane

The otolith system, utricle and saccule, is located in two small sacs within the inner ear labyrinth. Each sac hosts a sense organ, the macula, which contains the direction sensitive hair cells. Though it has been known for a long time that otoliths sense accelerations of the head, a detailed view of the mechanical properties has long been hampered by the problem of the fixation of otolith tissue (Lindeman, 1969).

Figure 4 sketches a cross section through an otolith organ (saccule) while figure 5 shows a micrograph of this area. Like in all other sensory systems of the inner ear, hair cells represent the sensory units which respond to displacements of the hair bundles by a change of excitation. They are firmly attached to the skull by connective tissue and covered by three consecutive layers of a morphologically separable meshwork (Kachar et al., 1990). Unfortunately, different authors have used different terms for these layers. The topmost otoconia-layer consists of a filament meshwork,

containing calcium carbonate crystals known as otoconia (Lins et al., 2000) (see figure (6)).
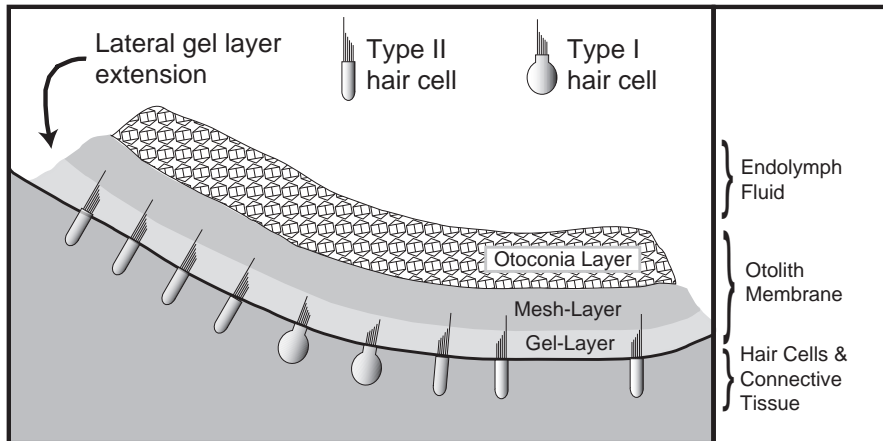
Figure 4: The layered structure of the otoliths. The figure also depicts the two kinds of hair cells found found in the macula, the sensory organ of the otoliths.
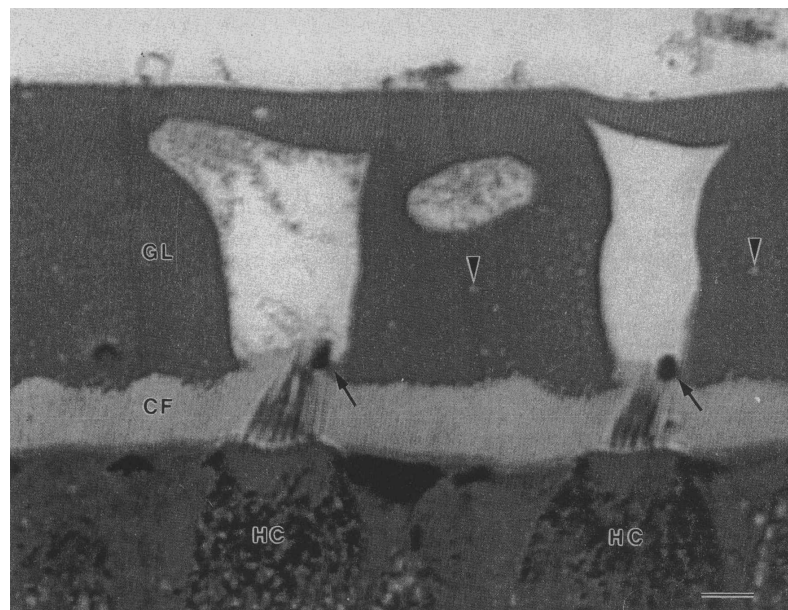
Figure 5: Light micrograph of a section of the otolith epithelium and membrane. The picture shows hair cells (HC), supporting cells, gel layer (CF) and the mesh layer (GL). The Otoconia and and their connecting filament were removed. Hair bundles originating from the hair cells and their attachment to the mesh layer (arrows) are visible along with cavities in the mesh layer above them. The scale bar has a length of $5.0\mu m$. (Taken from (Kachar et al., 1990); Courtesy of Elsevier).
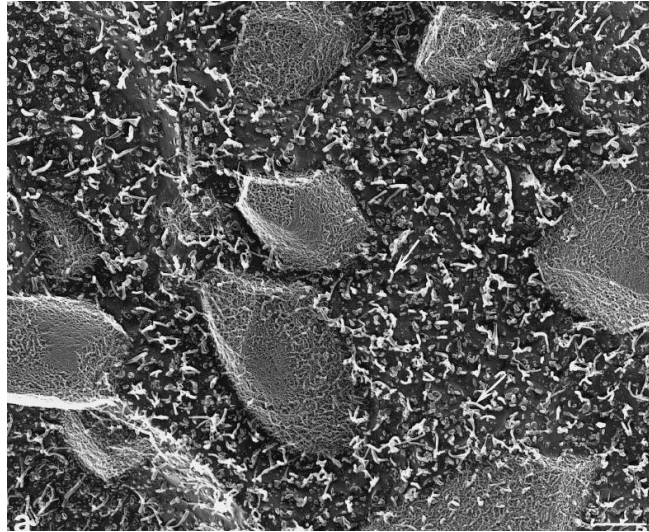
Figure 6: View of the otoconia embedded in the filament network. The scale bar has a length of $1.0\mu m$. (Taken from (Lins et al., 2000) with permission from Elsevier.)

Since the otoconia have a higher density than the underlying parts of the otolith membrane and the surrounding endolymph fluid, their position with respect to the sensory epithelium is displaced by accelerations. Recent findings indicate that the middle layer, which will be termed mesh-layer, is also relatively stiff (Benser et al., 1993; Kondrachuk, 2000). Structurally it consists of a densely and randomly interconnected filament matrix. Its function is probably to distribute the forces acting on the otoconia in a homogeneous fashion. The more elastic lower layer represents the main source of flexibility within the otolith membrane (Kondrachuk, 2000). It is connected to the apical surface of the macula. In comparison with the mesh-layer, its meshwork is less densely connected and exhibits a columnar structure (see figure 7). It's visco-elastic properties resembles those of a gel, and is therefore called gel-layer (Grant et al., 1984; Grant and Best, 1986, 1987; Grant and Cotton, 1990; Grant et al., 1993) (other names are columnar and sub-otolithic layer). A band like region in the center of the otoliths, known as *striola* can be distinguished (see Fig. 2). This regions exhibits different properties with respect to otoconia size (Lindeman, 1969), filament structure (Lim, 1976) and hair cell characteristics (Goldberg et al., 1990*b*).

If a constant acceleration is applied, for example by a tilt of the head, the otoconia will move until the buoyant force acting on them is counterbalanced by elastic forces that originate in the otolith membrane. The gel is commonly treated as a Kelvin-Voight fluid, i.e. a visco-elastic element with linear elasticity. Due to the structure of the system, forces parallel to the layers lead to a shear deflection of the gel layer, while perpendicular forces have virtually no effect. The curved shape of the otoliths ensures that for any direction of linear acceleration, at least some parts of them will
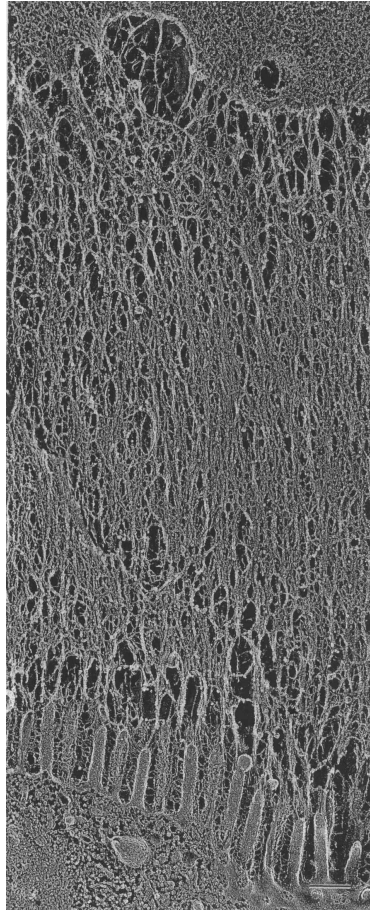
Figure 7: Filament structure of the gel layer (columnar filament layer) revealed by freeze etching. Microvilli are visible on the apical surface of the supporting cells in the lower part of the figure. In the upper part, the dens random meshwork of the mesh layer can be seen. The scale bar has a length of $0.5\mu m$. (Taken from (Kachar et al., 1990); Courtesy of Elsevier).

experience a shearing force. Therefore shape and orientation of the otoliths are of central interest for understanding their mechanical response.

The shape and orientation of the otolith maculae have been subject to dispute for a long time. Few attempts have been made to determine them quantitatively since the fixation of this structure is complicated. Probably the only measurements of human maculae are the ones by Takagi et al. and Sato et al. (Takagi and Sando, 1988; Sato et al., 1992). They employed a computer-aided technique to reconstruct temporal bone structures in fine detail from serial sections in three dimensions. The data sets used for simulation and visualization have been taken from these studies, and Figure 2 shows shape and position of the macula of the left utricle and saccule in stereotactic coordinates. The underlying surfaces were created by introducing new

data points, especially where the surfaces meet the coordinate axes. The result of this procedure was controlled visually. They are included to clarify the shape of the otoconia-covered area. Both figures are based on approximately 300 measured data-points, which have been subjected to a smoothing procedure. The original data set included even more points organized in rows along the sliced surface. Completely outlying rows were deleted, and rows that were obviously displaced with respect to the rest of the data were shifted to align with the other rows. The data set was further rotated to coincide with head stereotactic coordinates. This procedure made use of the orientation of the semicircular canals, which were also included in the data set and measurements of their orientation in man (Blanks et al., 1975). Based on the resulting data set, a representation on an equally spaced grid was created. We used a standard analytical program for this transformation (Igor Pro 3.14; WaveMetrics Inc.). The resulting geometry was then used for the figures as well as for the simulations. Fig. 2A shows that the whole utricular surface is tilted upward frontally by about 30°, with the tilt becoming larger anteriorly. The upper portion of the saccule macula (Fig. 2B) is largely parallel to the mid-sagittal plane (defined by dorso-ventral and anterior-posterior axes), while the lower part is tilted temporally. The position of the striola has been taken from observations by Lindeman (Lindeman, 1969). Curthoys et al. have obtained similar anatomical data sets for the otolith maculae of Guinea pigs (Curthoys et al., 1999). Their study also finds that the otoliths maculae are curved surfaces.

1.3 Hair cells

The hair cells of the otolith macula detect displacements within the otolith membrane. They come in two types: flask-like type I and spherical type II cells. Both cell types feature a bundle of interconnected short hairs named *stereocilia*, which are linked to one taller hair known as *kinocilium*. The length of the stereocilia thereby increases gradually in the direction to the kinocilium, giving the impression of a staircase. The stereocilia are embedded into the gel layer, while the kinocilia of the extra-striola area are attached to the mesh-layer (Kachar et al., 1990) or even protrude into the otoconia-layer above (Lim, 1976; Ross et al., 1987). For kinocilia in the striola region the attachment is not clear yet. The polarization of hair cells is determined by direction and magnitude of the deflection of the kinocilium (Shotwell et al., 1981): deflection of the hair bundle towards the kinocilium leads to a depolarization, and deflection in the opposite direction to a hyper-polarization of the hair cell. Investigations have suggested that the tip links are directly connected to mechanically gated transduction channels (Assad et al., 1991). Thus deflection of the hair bundles leads to a stretching of the tip links which in turn leads to an opening of the transduction channels.
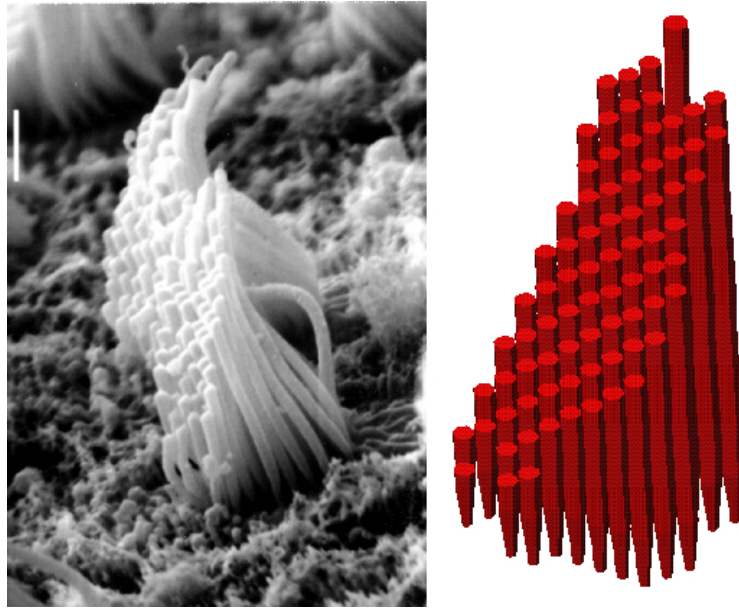
Figure 8: Scanning micrograph and reconstruction of a hair bundle (Courtesy of E. Peterson and W. Grant).

Hair cells are innervated by neurons located in Scarpa's ganglion, which lies in the internal auditory meatus. Generally hair cells are innervated by more than one neuron. Neurons further usually form connections with several hair cells. Besides afferent neurons, which transport information to the brain, they are also innervated by efferent neurons. This leads to a complex innervation pattern at the macula level. It is assumed that some processing of hair cell signals already occur at this stage. Because of this, investigations presented in this thesis are restricted to hair cell responses.

Hair cells can be distinguished by their innervation. Type I cell are contacted by a calyx ending which envelopes the cell body while type II cells are contacted by boutons. Investigations have suggested that vestibular neurons can be characterized by the types of hair cells they innervate (Fernandez et al., 1990). They are grouped into calyx units, which only innervate one or more type I cells, bouton units that exclusively feature bouton endings and dimorphic unit which show both types of contacts. While calyx units are chiefly found in the striola region, bouton units seem to be absent there. Dimorphic units can be found anywhere on the macula (Goldberg et al., 1990b). Depending on their location (striola or extra-striola region) units further exhibit tonic/phasic or tonic discharge properties.

Vestibular neurons show a resting discharge rate of about 80Hz (Goldberg and Fernandez, 1971). Deflections of the hair bundles lead to a modulation of this firing

rate. These neurons project mainly to the vestibular nucleus in the brain stem. The vestibular nucleus is thought to integrate information from different sensory inputs, namely the semi-circular canals, otoliths and vision. Some neurons project to the ipsilateral cerebellar cortex and one of the deep cerebellar nuclei. The study of the vestibular system may thus also reveal information about the cerebellum, since vestibular neurons are the only ones which have direct pathway to it.

2 Methods

Several analytical and numerical techniques were used to derive the properties of the stimulus transition, apparent in the otoliths. Mechanical responses of a 3D model of the otolith membrane were calculated in the static (time-independent) and dynamic (time-dependent) case using the method of finite elements (FEM). To this end a program was written which incorporates this method. Commercially available software (Abaqus 6.0, Abaqus Inc.) and an open source code (Calculix 0.92 by G. Dhondt and K. Wittig) were also employed in this investigation. A transfer function of a simplified model was developed and employed to validate these results. Fractional calculus was used to describe the response characteristics of tonic/phasic striola hair cells.

2.1 Continuum Mechanics

The theory of continuum mechanics forms the basis for the description of the mechanical properties of the otolith membrane. It involves the description of strain and stress within an extended body. Taken together a set of partial differential equations can be found which describe the mechanical responses of this body. Notations in this chapter were chosen similar to (Lai et al., 1993). Bold face letters specifically indicate vector quantities.

2.1.1 Strain

If a body undergoes deformation, parts of it get displaced with respect to its frame of reference. The deformed body may then be described with respect to its deformed (Eulerian description) or its initial configuration (Lagrangian description). Body coordinates x_i may further depend on time t. In Lagrangian description they can thus be indicated as:

$$x_i = x_i(\hat{x}_1, \hat{x}_2, \hat{x}_3, t)$$

Here letters with a hat indicate the initial configuration.

A body in a particular initial state at reference time t_1 is transformed to another configuration at t_2. Because of this, a point P (initially at location P_1 with coordinates $\hat{\mathbf{x}}$) is subject to a displacement $\mathbf{u}$, which results in a new location of that point at time t_2 (see Fig. 9):

$$\mathbf{x} = \hat{\mathbf{x}} + \mathbf{u}(\hat{\mathbf{x}}, t)$$

A point Q with the location $\hat{\mathbf{x}} + d\hat{\mathbf{x}}$ in the neighborhood of P is displaced to:

$$\mathbf{x} + d\mathbf{x} = \hat{\mathbf{x}} + d\hat{\mathbf{x}} + \mathbf{u}(\hat{\mathbf{x}} + d\hat{\mathbf{x}}, t)$$

After subtraction of these equation one obtains:
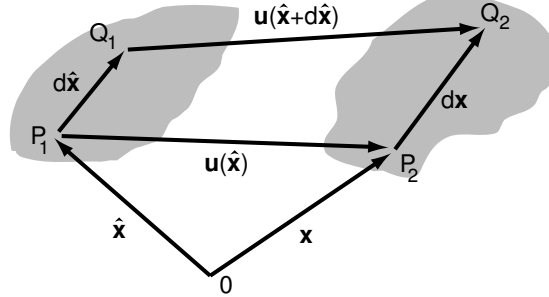
Figure 9: Deformation of a body. The figure illustrates the changes, due to deformation within the body.

$$d\mathbf{x} = d\hat{\mathbf{x}} + \mathbf{u}(\hat{\mathbf{x}} + d\hat{\mathbf{x}}, t) - \mathbf{u}(\hat{\mathbf{x}}, t)$$

or

$$d\mathbf{x} = d\hat{\mathbf{x}} + (\nabla\mathbf{u})d\hat{\mathbf{x}}$$

This may be rewritten to:

$$d\mathbf{x} = \mathbf{F}d\hat{\mathbf{x}} \tag{1}$$

with

$$\mathbf{F} = \mathbf{I} + \nabla\mathbf{u}$$

To find the relationship between the length of $d\mathbf{x}$ and $d\hat{\mathbf{x}}$ one takes the dot product of equation (1) with itself. This results in:

$$(ds)^2 = d\mathbf{x} \cdot d\mathbf{x} = d\hat{\mathbf{x}}^T \mathbf{F}^T \mathbf{F} d\hat{\mathbf{x}} \tag{2}$$

with

$$\mathbf{F}^T\mathbf{F} = (\mathbf{I} + \nabla\mathbf{u})^T(\mathbf{I} + \nabla\mathbf{u}) = \mathbf{I} + \nabla\mathbf{u} + (\nabla\mathbf{u})^T + (\nabla\mathbf{u})^T\nabla\mathbf{u} \tag{3}$$

The components of $(\nabla\mathbf{u})^T\nabla\mathbf{u}$ are small quantities of higher order than the components of $\nabla\mathbf{u}$. If these higher order elements are neglected, equation (3) becomes:

$$\mathbf{F}^T\mathbf{F} \approx \mathbf{I} + \nabla\mathbf{u} + (\nabla\mathbf{u})^T = \mathbf{I} + 2\mathbf{E} \tag{4}$$

$\mathbf{E}$ is known as infinitesimal strain tensor. The components of this tensor in rectangular coordinates are:

$$E_{ij} = \frac{1}{2}\left(\frac{\partial u_i}{\partial \hat{x}_j} + \frac{\partial u_j}{\partial \hat{x}_i}\right) \tag{5}$$

or

$$[E] = \begin{bmatrix} \dfrac{\partial u_1}{\partial \hat{x}_1} & \dfrac{1}{2}\left(\dfrac{\partial u_1}{\partial \hat{x}_2} + \dfrac{\partial u_2}{\partial \hat{x}_1}\right) & \dfrac{1}{2}\left(\dfrac{\partial u_1}{\partial \hat{x}_3} + \dfrac{\partial u_3}{\partial \hat{x}_1}\right) \\[3mm] \dfrac{1}{2}\left(\dfrac{\partial u_1}{\partial \hat{x}_2} + \dfrac{\partial u_2}{\partial \hat{x}_1}\right) & \dfrac{\partial u_2}{\partial \hat{x}_2} & \dfrac{1}{2}\left(\dfrac{\partial u_2}{\partial \hat{x}_3} + \dfrac{\partial u_3}{\partial \hat{x}_2}\right) \\[3mm] \dfrac{1}{2}\left(\dfrac{\partial u_1}{\partial \hat{x}_3} + \dfrac{\partial u_3}{\partial \hat{x}_1}\right) & \dfrac{1}{2}\left(\dfrac{\partial u_2}{\partial \hat{x}_3} + \dfrac{\partial u_3}{\partial \hat{x}_2}\right) & \dfrac{\partial u_3}{\partial \hat{x}_3} \end{bmatrix} \tag{6}$$

Geometrically, diagonal elements of (6) represent the unit elongation (i.e. the increase in length per unit original length) of an material element which was originally in the $d\hat{x}_i$ direction (see Fig. 9):

$$\frac{ds - d\hat{s}}{d\hat{s}} = E_{ii}$$

Here $d\hat{s}$ and ds are the lengths of $d\hat{x}_i$ before and after deformation of the body. Off-diagonal elements E_{ij} can be identified with the change of angle γ_{ij} between two material elements $d\hat{x}_i$ and $d\hat{x}_j$ which were originally perpendicular to each other:

$$\gamma_{ij} = 2E_{ij}$$

The change of angle is also known as shear strain, while the unit elongation due to diagonal elements is termed normal strain.

The infinitesimal strain tensor is important since it enters into the stress-strain relationship.

2.1.2   Stress

Continuum mechanics is concerned with the motion and displacement properties of extended bodies. To describe these properties in the form of differential equations, small volumes of the body are considered. Forces acting on these volumes are distributed over its surfaces. Because of this, they are described in terms of stress vectors, which incorporate the size of a surface. Stress vectors $\mathbf{t_n}$ are defined as:

$$\mathbf{t_n} = \lim_{\Delta A \to 0} \frac{\Delta \mathbf{F}}{\Delta A} \tag{7}$$

Here $\Delta \mathbf{F}$ indicates the force acting on a small surface ΔA. According to Chauchy's stress principle, the stress vector on a surface depends only on the unit normal vector $\mathbf{n}$ to the surface. It has been found that the stress vector can be described in terms of $\mathbf{n}$:

$$\mathbf{t_n} = \mathbf{Tn} \tag{8}$$

In this formula $\mathbf{T}$ represents a tensor which transforms the unit normal vector into the stress vector. $\mathbf{T}$ is known as stress tensor. Diagonal elements of $\mathbf{T}$ are normal stresses to the surface, while off-diagonal elements represent shearing stresses. For the components of the unit normal vector of the surface this may also be written as:

$$\mathbf{t}_{\mathbf{e}_i} = \mathbf{T}\mathbf{e}_i \tag{9}$$

2.1.3 Stress-Strain Relationship

According to Hook's law, stresses within a body can be described in terms of body strains, i.e. $\mathbf{T} = \mathbf{T}(\mathbf{E})$ with $\mathbf{T}$ and $\mathbf{E}$ being the stress and strain tensor, respectively. With respect to a basis $\mathbf{e}_i$ the relation between $\mathbf{T}$ and $\mathbf{E}$ for a linear elastic solid can be stated as (using the Einstein summation convention):

$$T_{ij} = C_{ijkl}E_{kl} \tag{10}$$

Here C_{ijkl}, the elasticity tensor, is a fourth order tensor that describes the relation between stress and strain. In the case of an isotropic material equation (10) can be simplified to:

$$T_{ij} = C_{ijkl}E_{kl} = \lambda(E_{11} + E_{22} + E_{33}) + 2\mu E_{ij} = \lambda e\delta_{ij} + 2\mu E_{ij} \tag{11}$$

or

$$\mathbf{T} = \lambda e\mathbf{I} + 2\mu\mathbf{E} \tag{12}$$

Here e indicates the trace of the strain tensor and λ and μ are the Lame's constants. The constant μ is also known as as shear modulus. These constants determine the mechanical deformation of the body. More commonly in use than the Lame' constants are Young's modulus E_y and the Poisson ratio ν. They are related to each other by:

$$E_y = \frac{\mu(3\lambda + 2\mu)}{\lambda + \mu} \tag{13}$$

$$\nu = \frac{\lambda}{2(\lambda + \mu)} \tag{14}$$

If the stress and strain tensor are written in vector form and renamed to $\boldsymbol{\tau}$ and $\boldsymbol{\epsilon}$, equation (12) can also be stated as:

$$\boldsymbol{\tau} = [D]\boldsymbol{\epsilon} \tag{15}$$

where

$$\boldsymbol{\tau} = \begin{pmatrix} T_{11} \\ T_{22} \\ T_{33} \\ T_{12} \\ T_{23} \\ T_{13} \end{pmatrix} \qquad \boldsymbol{\epsilon} = \begin{pmatrix} E_{11} \\ E_{22} \\ E_{33} \\ 2E_{12} \\ 2E_{23} \\ 2E_{13} \end{pmatrix}$$

and

$$[D] = \frac{E_y}{(1+v)(1-2v)} \begin{pmatrix} 1-v & v & v & 0 & 0 & 0 \\ v & 1-v & v & 0 & 0 & 0 \\ v & v & 1-v & 0 & 0 & 0 \\ 0 & 0 & 0 & \frac{1-2v}{2} & 0 & 0 \\ 0 & 0 & 0 & 0 & \frac{1-2v}{2} & 0 \\ 0 & 0 & 0 & 0 & 0 & \frac{1-2v}{2} \end{pmatrix} \tag{16}$$

This form of the stress-strain relationship will be used in the further development of the finite element formulation.

2.1.4 Equation of the moving continuum

It is assumed that the movement of each particle of a continuum can be described according to Newton's second law. The particle may be viewed as a small cube in rectangular coordinates (see Fig. 10). The forces acting on it are due to the stresses on its six surfaces. In addition, body forces like weight may exist. Based on this, the equation of motion of a small volume filled with material of density ρ can be stated as:

$$\rho \mathbf{a} \Delta x_1 \Delta x_2 \Delta x_3 \;=\; \rho_{eff} \mathbf{B} \Delta x_1 \Delta x_2 \Delta x_3$$

$$+ \left(\frac{\mathbf{t}_{\mathbf{e}_1}(x_1 + \Delta x_1, x_2, x_3) - \mathbf{t}_{\mathbf{e}_1}(x_1, x_2, x_3)}{\Delta x_1} \right) \Delta x_1 \Delta x_2 \Delta x_3$$

$$+ \left(\frac{\mathbf{t}_{\mathbf{e}_2}(x_1, x_2 + \Delta x_2, x_3) - \mathbf{t}_{\mathbf{e}_2}(x_1, x_2, x_3)}{\Delta x_2} \right) \Delta x_1 \Delta x_2 \Delta x_3$$

$$+ \left(\frac{\mathbf{t}_{\mathbf{e}_3}(x_1, x_2, x_3 + \Delta x_3) - \mathbf{t}_{\mathbf{e}_2}(x_1, x_2, x_3)}{\Delta x_3} \right) \Delta x_1 \Delta x_2 \Delta x_3$$

Here $\mathbf{t}_{\mathbf{e}_i}$ are stress vectors acting on the cube surface with direction i. The cube is further characterized by the side lengths Δx_i. Inertial forces are proportional the

acceleration **a** of the body. **B** is an external acceleration which leads to a force proportional to the effective density ρ_{eff}. This density is the difference between the density of the body and the density of the material surrounding it.
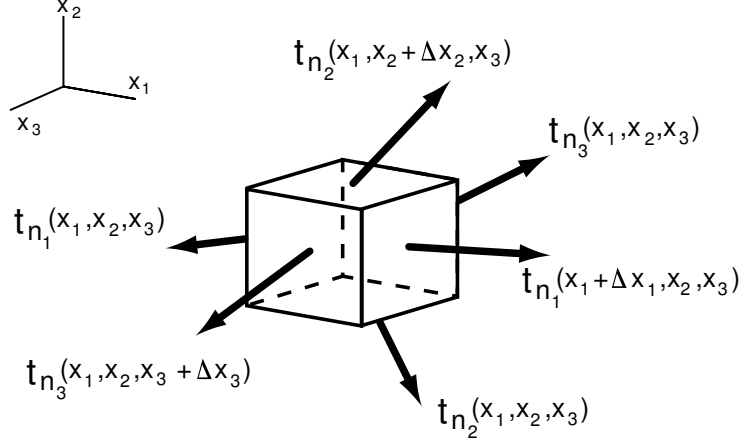
Figure 10: Stress vectors on the faces of a small cubic volume with side lengths Δx_1, Δx_2 and Δx_3.

If the equation above is divided by the Δx_i and on letting $\Delta x_i \to 0$, we obtain:

$$\frac{\partial \mathbf{t_{e_1}}}{\partial x_1} + \frac{\partial \mathbf{t_{e_2}}}{\partial x_2} + \frac{\partial \mathbf{t_{e_3}}}{\partial x_3} + \rho_{eff}\mathbf{B} = \rho\mathbf{a} \tag{17}$$

Because of the relation between the stress vector and the stress tensor indicated in equation (9), equation (17) can also be stated as:

$$\frac{\partial T_{ij}}{\partial x_j} + \rho_{eff}B_i = \rho a_i \tag{18}$$

or in vector notation:

$$\mathrm{div}\mathbf{T} + \rho_{eff}\mathbf{B} = \rho\mathbf{a} \tag{19}$$

For a linear elastic and isotropic material, the stress tensor **T** can be expressed in terms of the strain tensor (equation (11):

$$T_{ij} = \lambda e\delta_{ij} + 2\mu E_{ij} = \lambda e\delta_{ij} + \mu\left(\frac{\partial u_i}{\partial x_j} + \frac{\partial u_i}{\partial x_j}\right) \tag{20}$$

After differentiation of this equation with respect to x_j, one obtains:

$$\frac{\partial T_{ij}}{\partial x_j} = \lambda\frac{\partial e}{\partial x_j}\delta_{ij} + \mu\left(\frac{\partial^2 u_i}{\partial x_j\partial x_j} + \frac{\partial^2 u_j}{\partial x_j\partial x_j}\right) \tag{21}$$

It can further be found that

$$\frac{\partial e}{\partial x_j}\delta_{ij} = \frac{\partial e}{\partial x_i} \tag{22}$$

and

$$\frac{\partial^2 u_j}{\partial x_j \partial x_i} = \frac{\partial}{\partial x_i}\left(\frac{\partial u_j}{\partial x_j}\right) = \frac{\partial e}{\partial x_i} \tag{23}$$

were

$$e = \frac{\partial u_i}{\partial x_i} = \frac{\partial u_1}{\partial x_1} + \frac{\partial u_2}{\partial x_2} + \frac{\partial u_3}{\partial x_3}$$

By combining equation (21),(22),(23), the derivative of the stress tensor in equation (18) can be substituted and the equation of motion can be stated as:

$$\rho\frac{\partial^2 u_i}{\partial t^2} = \rho_{eff}B_i + (\lambda + \mu)\frac{\partial e}{\partial x_i} + \mu\frac{\partial^2 u_i}{\partial x_j \partial x_j} \tag{24}$$

These equations for the description of the moving continuum are known as Navier's equations. They can be stated in invariant form as:

$$\rho\frac{\partial^2 \mathbf{u}}{\partial t^2} = \rho_{eff}\mathbf{B} + (\lambda + \mu)\nabla e + \mu\text{div}\nabla\mathbf{u} \tag{25}$$

with

$$e = \text{div}\mathbf{u}$$

Navier's equation does not account for damping effects. Damping may be introduced by inserting velocity dependent terms into equation (25). These terms are analogous to the terms that describe the elastic behavior of the material. This assumption is applicable if the material can be characterized by isotropic, linear damping. It further implies that the stress-strain relation of the material is time independent. In addition to the Lame' constants, further parameters are needed that characterize damping. Equation (25) then becomes:

$$\begin{aligned}\rho\frac{\partial^2 \mathbf{u}}{\partial t^2} = \rho_{eff}\mathbf{B} \quad &+ \quad (\lambda_{ela} + \mu_{ela})\nabla e + \mu_{ela}\text{div}\nabla\mathbf{u} \\ &+ \quad (\lambda_{visc} + \mu_{visc})\nabla\dot{e} + \mu_{visc}\text{div}\nabla\dot{\mathbf{u}}\end{aligned} \tag{26}$$

with

$$\dot{e} = \text{div}\dot{\mathbf{u}}$$

The Lame' constants λ and μ are here renamed to λ_{ela} and μ_{ela} to indicate their relationship to the elastic properties of the material. Materials that exhibit elastic

as well as damping characteristics are commonly referred to as visco-elastic materials, with the velocity-dependent parameters λ_{visc} and μ_{visc}.

In the case of time-independent problems the left hand side of equation (25) (i.e. the part related to acceleration) is set to zero and equation to be solved becomes:

$$0 = \rho_{eff}\mathbf{B} + (\lambda_{ela} + \mu_{ela})\nabla e + \mu_{ela}\mathrm{div}\nabla\mathbf{u} \tag{27}$$

The static and dynamic properties of the otolith membrane can be described using equations (27) and (26).

2.2 The Finite Element Method (FEM)

The static and dynamic properties of the otolith membrane were studied using the method of finite elements. During the last decades this method has found numerous applications, for instance in fluid dynamics, head transfer problems and electro dynamics. It is used here to model the displacement of the otolith membrane due to externally applied accelerations in various directions. The finite element technique is especially well suited for this problem, since the irregular boundaries of the macula pose no problem to this technique.

In a first step the object to be simulated is broken down into a set of smaller volumes, in our case hexahedrons (i.e. cubes) or tetrahedrons. The next step is to implement the numerical representation of the differential equation. Central to the finite element technique is the piecewise representation of the desired function, i.e. the solution to the differential equation, with simple approximating functions. In our simulations the solution to the differential equation was represented by a set of three linear or quadratic functions (one for each spatial dimension) for each element. At the corners of the elements, also called nodes, those approximating functions must match to form a continuous overall solution. These matching conditions fix the coefficients that characterize the approximating functions. Numerically this leads to a system of linear equations. As a result one obtains the 3D node displacements due to body forces, i.e. forces distributed over the hexahedrons, due to the external acceleration. Special conditions apply at the surface of the simulated volume: the nodes at the gel-skull boundary are not allowed to move, which reflects the tight connection between otolith gel and skull. No interaction is assumed at the border with the endolymph fluid. As the number of elements or the set of coefficients (using a higher order polynomial) is increases, the approximation gets better. But there are limitations to the increase of spatial resolution since the size of the resulting linear equations rises very rapidly in 3D problems.

The formulation of the method is different for time-independent and time-dependent cases. For the latter case an additional time integration has to be performed. Various numerical schemes are in use for this purpose. The derivation of the finite element method was influenced by (Rao, 1982) and (Bathe and Wilson, 1976).

2.2.1   The Discretization Process

The first step in the application of the finite element method is the discretization of the relevant domain into subregions (finite elements). This involves the choice of appropriate element types. In general hexahedrons with quadratic approximation functions (i.e. the three functions to approximate the three-dimensional displacement of the element) were used in this investigation. Additionally cubes and tetrahedrons with a linear approximation function were employed for validation purposes. Hexahedron elements are especially suited for this problem since they are less prone to an numerical artefact known as *locking*. Element shapes were chosen in such a way that they did not cross the borders between membrane layers. Because of this, the mechanical properties of every element were determined by the layer it belonged to. This yields a layered structure of the membrane, which is reflected by the layered arrangement of the elements.

The construction of the discretization was based on the curved shape of the otolith macula. An initial two-dimensional discretization was created manually by adjusting a quadrilateral mesh on the curved macula. This mesh was subject to two conditions. First it was required that all inner angles of the quadrilaterals were close to 90°. This ensures the accuracy of the finite element solution. Second the whole macula area needed to be covered with the quadrilaterals. Based on this initial mesh the three-dimensional discretization of the otolith membrane was constructed. The nodes at the corners of the quadrilaterals thereby served as the corners of the cubes for one side of the lowest layer of hexahedrons. Similar to the conditions imposed on the quadrilaterals it computationally desirable that the inner angles of adjacent cube sides are close to 90°.

The nodes at the edges of the cubes were constructed by taking the cross product of the side vectors defined by the quadrilateral discretization. This leads to a vector perpendicular to the surface of a quadrilateral. Since a minimum of one and a maximum of four quadrilaterals border on a node of the quadrilateral mesh, a compromise vector was calculated to account for the different orientations of the different quadrilaterals. The arithmetic mean of the vector components served for this purpose. Based on this vector, the edges of the cubes were calculated in a way that ensured that every element belonged only to one type of material. Since the otoconia layer deflections are mediated by the mesh layer and the displacements of

this layer are small, each was discretized by one layer of finite elements. The gel
layer was further subdivided into two or three element sub-layers. This was done
to ensure appropriate results especially in the case of dynamical situations. The
resulting discretization of the utricular and saccular otolith membrane can be seen
in Fig. 11 and Fig. 12. This hexahedron grid also served as the basis for tetrahedron
discretization. In this case the cubes were further broken down into sets of five
tetrahedrons.
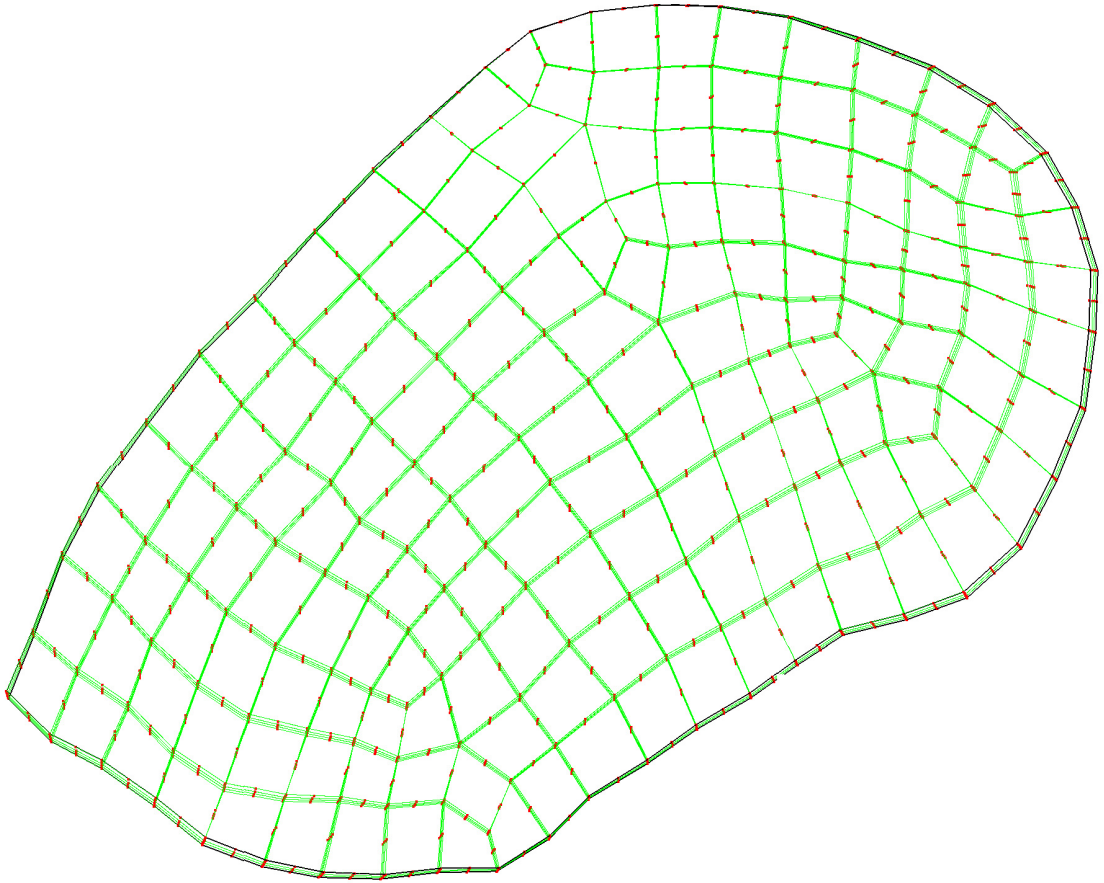
Figure 11: Hexahedron discretization of the utricular otolith membrane. Small dots indicate the
position of the nodes.
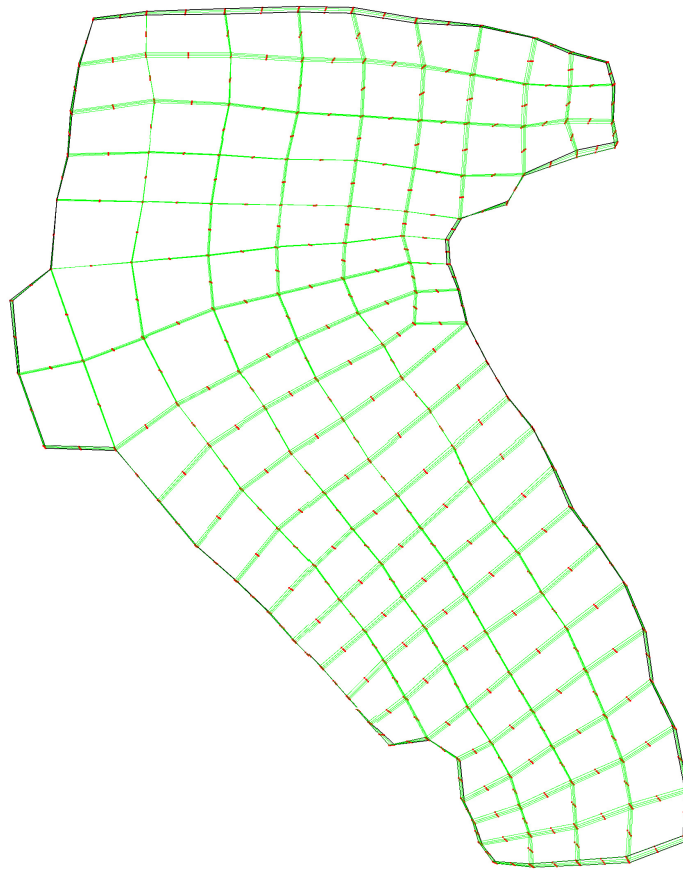
Figure 12: Hexahedron discretization of the saccular otolith membrane. Small dots indicate the position of the nodes.

2.2.2   Shape functions

The finite element method rests on piecewise approximations of the solution of a differential equation. For a complicated problem this means that the region of interest is subdivided into smaller volumes (i.e. finite elements) and the solution within this subregion is approximated by simple functions known as shape functions. Two methods are in use to derive the shape functions. One is based on the global coordinate system, while the other employs element specific local coordinates. Commonly in use for this purpose are polynomials with an order up to three. In the case of a linear approximation of a three dimensional problem, the approximation function of a scalar field variable $\phi(x, y, z)$ becomes in the global coordinate system:

$$\phi(x, y, z) = \alpha_1 + \alpha_2\ x + \alpha_3\ y + \alpha_4\ z \tag{28}$$

and for a quadratic approximation:

$$\begin{aligned}
\phi(x, y, z) = \alpha_1 &+ \alpha_2\ x + \alpha_3\ y + \alpha_4\ z \\
&+ \alpha_5\ x^2 + \alpha_6\ y^2 + \alpha_7\ z^2 \\
&+ \alpha_8\ xy + \alpha_9\ yz + \alpha_{10}\ xz
\end{aligned} \tag{29}$$

The coefficients α_i of equation (28) and (29) can now be expressed in terms of the global coordinates and the values of the approximation functions at the nodes.

a) Linear tetrahedron shape functions

For a linear tetrahedron element this is carried out as follow (see Figure 13).
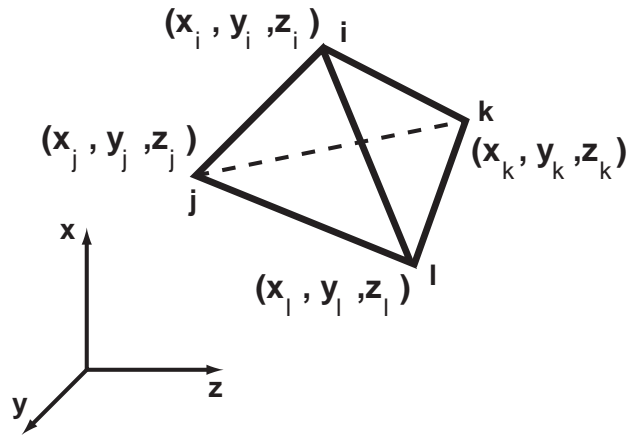
Figure 13: Coordinates of a tetrahedron element.

At the four nodes (named i,j,k,l) equation (28) becomes:

$$\phi_i = \alpha_1 + \alpha_2\, x_i + \alpha_3\, y_i + \alpha_4\, z_i$$
$$\phi_j = \alpha_1 + \alpha_2\, x_j + \alpha_3\, y_j + \alpha_4\, z_j$$
$$\phi_k = \alpha_1 + \alpha_2\, x_k + \alpha_3\, y_k + \alpha_4\, z_k$$
$$\phi_l = \alpha_1 + \alpha_2\, x_l + \alpha_3\, y_l + \alpha_4\, z_l$$

These are four equations which can be solved for the four unknown $\alpha's$. They can be expressed as:

$$\alpha_1 = \frac{1}{6V}(a_i\phi_i + a_j\phi_j + a_k\phi_k + a_l\phi_l)$$

$$\alpha_2 = \frac{1}{6V}(b_i\phi_i + b_j\phi_j + b_k\phi_k + b_l\phi_l)$$

$$\alpha_3 = \frac{1}{6V}(c_i\phi_i + c_j\phi_j + c_k\phi_k + c_l\phi_l)$$

$$\alpha_4 = \frac{1}{6V}(d_i\phi_i + d_j\phi_j + d_k\phi_k + d_l\phi_l)$$

where V is the volume of the tetrahedron. The volume and the coefficients are given by:

$$V = \frac{1}{6}\begin{vmatrix} 1 & x_i & y_i & z_i \\ 1 & x_j & y_j & z_j \\ 1 & x_k & y_k & z_k \\ 1 & x_l & y_l & z_l \end{vmatrix} \tag{30}$$

$$a_i = \begin{vmatrix} x_j & y_j & z_j \\ x_k & y_k & z_k \\ x_l & y_l & z_l \end{vmatrix} \qquad\qquad b_i = -\begin{vmatrix} 1 & y_j & z_j \\ 1 & y_k & z_k \\ 1 & y_l & z_l \end{vmatrix}$$

$$c_i = \begin{vmatrix} x_j & 1 & z_j \\ x_k & 1 & z_k \\ x_l & 1 & z_l \end{vmatrix} \qquad\qquad d_i = -\begin{vmatrix} x_j & y_j & 1 \\ x_k & y_k & 1 \\ x_l & y_l & 1 \end{vmatrix}$$

The other coefficients are obtained by cyclic permutation of the indices.

This results can now be substituted into equation (28):

$$\phi(x,y,z) = N_i(x,y,z)\phi_i + N_j(x,y,z)\phi_j + N_k(x,y,z)\phi_k + N_l(x,y,z)\phi_l \tag{31}$$
$$= [N(x,y,z)]\phi^{(e)} \tag{32}$$

The field variable $\phi(x, y, z)$ is therefore expressed in terms of the vector of nodal values $\boldsymbol{\phi}^{(e)}$ with:

$$[N(x, y, z)] = [N_i(x, y, z) \ N_j(x, y, z) \ N_k(x, y, z) \ N_l(x, y, z)] \tag{33}$$

$$N_i(x, y, z) = \frac{1}{6V}(a_i + b_i x + c_i y + d_i z)$$

$$N_j(x, y, z) = \frac{1}{6V}(a_j + b_j x + c_j y + d_j z)$$

$$N_k(x, y, z) = \frac{1}{6V}(a_k + b_k x + c_k y + d_k z)$$

$$N_l(x, y, z) = \frac{1}{6V}(a_l + b_l x + c_l y + d_l z) \tag{34}$$

and

$$\boldsymbol{\phi}^{(e)} = \begin{pmatrix} \phi_i \\ \phi_j \\ \phi_k \\ \phi_l \end{pmatrix}$$

This representation of the field variable (with an extension to a vector quantity $\boldsymbol{\phi}(x, y, z)$ is then used in the variational formulation of the mechanical-displacement problem. The functions $N_i \ldots N_k$ relate the field variable $\phi(x, y, z)$ to the nodal values of the variable. They are called *shape functions* and form a matrix with the dimension 1 x n, were n is the number of element nodes.

b) Quadratic hexahedron shape functions

Another, more general method to derive shape functions rests on the transformation to a local coordinate system for the elements. Using a linear transformation, a distorted hexahedron can be mapped onto a non-distorted cube with unit side lengths (Fig. 14). In this process the variables x, y and z are transformed to the variables r, s and t of the natural coordinate system.

The advantage of this procedure rests on the fact that in the later stage of finite element analysis integrations over the volume of the element need to be carried out, which is much easier to perform in the non-distorted case. Figure 14 shows this transformation to natural coordinates for a 20-node cube element. This element has found a particularly wide range of applications in conjecture with a quadratic approximation function (Eqn. (29)). If the origin of the natural coordinate system is put into the center of the cube, the mapping for a 20-node cube element can be stated as:

$$x = \sum_{i=1}^{20} N_i x_i; \qquad y = \sum_{i=1}^{20} N_i y_i; \qquad z = \sum_{i=1}^{20} N_i z_i; \tag{35}$$
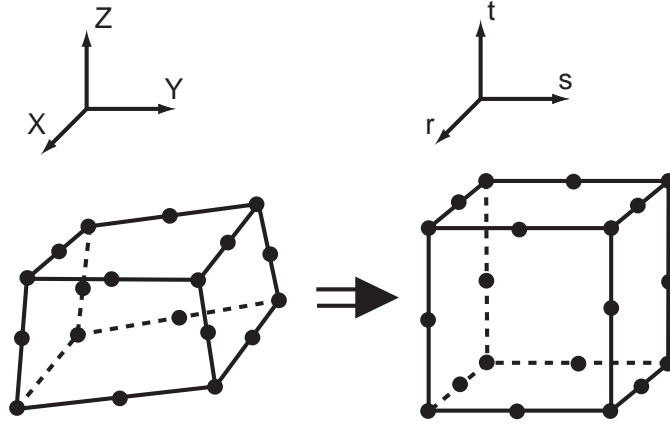
Figure 14: Transformation to natural coordinates for a 20-node cube element.

or

$$\begin{pmatrix} x \\ y \\ z \end{pmatrix} = \begin{bmatrix} N_1 & \dots & N_{20} & 0 & \dots & 0 & 0 & \dots & 0 \\ 0 & \dots & 0 & N_1 & \dots & N_{20} & 0 & \dots & 0 \\ 0 & \dots & 0 & 0 & \dots & 0 & N_1 & \dots & N_{20} \end{bmatrix} \begin{pmatrix} x_1 \\ \vdots \\ x_{20} \\ y_1 \\ \vdots \\ y_{20} \\ z_1 \\ \vdots \\ z_{20} \end{pmatrix}$$

Thus the coordinates inside the cube are written as a function of the node coordinates. Thereby the shape functions N_i at the corner nodes ($i = 1 \dots 8$; see Fig. 15) are given as:

$$N_i = \frac{1}{8}(1 + rr_i)(1 + ss_i)(1 + tt_i)(rr_i + ss_i + tt_i - 2) \tag{36}$$

where r_i, s_i and t_i can take on the values ± 1. At the mid-side nodes $i = 9, 11, 17, 19$:

$$N_i = \frac{1}{4}(1 - r^2)(1 + ss_i)(1 + tt_i)) \tag{37}$$

where s_i and t_i can take on the values ± 1. At the mid-side nodes $i = 10, 12, 18, 20$:

$$N_i = \frac{1}{4}(1 - s^2)(1 + rr_i)(1 + tt_i)) \tag{38}$$

where r_i and t_i can take on the values ± 1. At the mid-side nodes $i = 13, 14, 15, 16$:

$$N_i = \frac{1}{4}(1 - t^2)(1 + rr_i)(1 + ss_i)) \tag{39}$$

where r_i and s_i can take on the values ± 1.

These shape functions N_1 are also used the characterize the magnitude of the field variable $\phi(x, y, z)$:

$$\phi(x, y, z) = [N]\boldsymbol{\phi}^{(e)} = [N_1 \quad \ldots \quad N_{20}]\boldsymbol{\phi}^{(e)}$$

where

$$\boldsymbol{\phi}^{(e)} = \begin{pmatrix} \phi_1(x_1, y_1, z_1) \\ \vdots \\ \phi_{20}(x_{20}, y_{20}, z_{20}) \end{pmatrix}$$
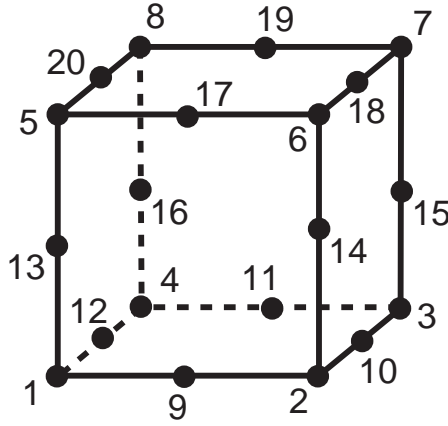
Figure 15: Node numbering of the 20-node cube element.

Using these equations, a scalar quantity like temperature can be approximated within an element. In the case of a vector quantity like displacement, the field variable ϕ is generalized to a vector function (3-dimensional case):

$$\boldsymbol{\phi}(x, y, z) = \begin{pmatrix} \phi_x(x, y, z) \\ \phi_y(x, y, z) \\ \phi_z(x, y, z) \end{pmatrix} =: \begin{pmatrix} u(x, y, z) \\ v(x, y, z) \\ w(x, y, z) \end{pmatrix} \tag{40}$$

Individual components of this vector function still employ the same shape functions as used for a scalar quantity. As a result, the vector of nodal values of the field variable has a dimension of 3n, were n is the number of element nodes. Correspondingly the shape functions are organized in a matrix with the dimension 3 x 3n.

2.2.3   Derivation of the Finite Element Method - Static Case

The finite element method is built on variational methods. This means that the underlying differential equation is solved by finding an extremal value of a corresponding functional. While there are several formulations in use, the following derivation of the finite element method in the static case will focus on the principle of minimum potential energy.

The potential energy π_p of an elastic body is defined as:

$$\pi_p = \pi - W_p \tag{41}$$

with π being the strain energy and W_p the work done on the body by external forces. The principle of minimum potential energy states that of all possible displacements that are compatible with the boundary conditions, the state which will be assumed makes the potential energy take on a minimum value. This state is called the equilibrium and the variation of equation (41) becomes zero:

$$\delta\pi_p = \delta\pi - \delta W_p = 0 \tag{42}$$

The total strain energy stored in a linear elastic body is:

$$\pi = \frac{1}{2} \iiint\limits_V \boldsymbol{\epsilon}^T \boldsymbol{\tau} dV \tag{43}$$

were $\boldsymbol{\tau}$ is the vector of stress components, $\boldsymbol{\epsilon}$ the vector of body strains (see Chapter (2.1.3)) and V is the volume of the body. By using equation (15) and assuming no initial stresses, the strain energy is expressed as:

$$\pi = \frac{1}{2} \iiint\limits_V \boldsymbol{\epsilon}^T [D] \boldsymbol{\epsilon} dV \tag{44}$$

External forces can be due to forces acting on the surface of a body or body forces. Body forces might act on any part of a body, like gravity. The work done by external forces is expressed as:

$$W_p = \iiint\limits_V (u\psi_{b_x} + v\psi_{b_y} + w\psi_{b_z})dV + \iint\limits_S (u\psi_{s_x} + v\psi_{s_y} + w\psi_{s_z})dS \tag{45}$$

or

$$W_p = \iiint\limits_V (\mathbf{U})^T \boldsymbol{\psi}_b dV + \iint\limits_S (\mathbf{U})^T \boldsymbol{\psi}_s dS \tag{46}$$

with $\boldsymbol{\psi}_b$ being the vector of known body forces and $\boldsymbol{\psi}_s$ the vector of surface forces. Displacements due to these forces are indicated by the vector

$$\mathbf{U}(x, y, z) = \begin{pmatrix} u(x, y, z) \\ v(x, y, z) \\ w(x, y, z) \end{pmatrix} \tag{47}$$

By substituting equation (44) and (46) into equation (41), the potential energy of a body can be described as:

$$\pi_p(u, v, w) = \frac{1}{2} \iiint\limits_V \boldsymbol{\epsilon}^T[D]\boldsymbol{\epsilon}\, dV - \iiint\limits_V (\mathbf{U})^T \boldsymbol{\psi}_b\, dV - \iint\limits_S (\mathbf{U})^T \boldsymbol{\psi}_s\, dS \tag{48}$$

The problem is now to find a displacement field $\mathbf{U}$ that minimizes the potential energy π_p.

If the body is discretized into a set of N finite elements, equation (48) holds for each element separately and the total potential energy is the sum of element potential energies:

$$\pi_p = \sum_{e=1}^{N} \pi_p^{(e)}$$

were $\pi_p^{(e)}$ is the element potential energy. Equation (48) can now be restated for a single element e as:

$$\pi_p^{(e)} = \frac{1}{2} \iiint\limits_{V^{(e)}} \boldsymbol{\epsilon}^T[D]\boldsymbol{\epsilon}\, dV - \iiint\limits_{V^{(e)}} (\mathbf{U})^T \boldsymbol{\psi}_b\, dV - \iint\limits_{S^{(e)}} (\mathbf{U})^T \boldsymbol{\psi}_s\, dS \tag{49}$$

Using shape functions and equation (6), the strain vector $\boldsymbol{\epsilon}$ can now be expressed in terms of the nodal displacement vector $\boldsymbol{\phi}^{(e)}$:

$$\boldsymbol{\epsilon} = \begin{pmatrix} \epsilon_{xx} \\ \epsilon_{yy} \\ \epsilon_{zz} \\ \epsilon_{xy} \\ \epsilon_{yz} \\ \epsilon_{xz} \end{pmatrix} = \begin{pmatrix} \frac{\partial u}{\partial x} \\ \frac{\partial v}{\partial y} \\ \frac{\partial w}{\partial z} \\ \frac{\partial u}{\partial y} + \frac{\partial v}{\partial x} \\ \frac{\partial v}{\partial z} + \frac{\partial w}{\partial y} \\ \frac{\partial w}{\partial x} + \frac{\partial u}{\partial z} \end{pmatrix} = \begin{pmatrix} \frac{\partial}{\partial x} & 0 & 0 \\ 0 & \frac{\partial}{\partial y} & 0 \\ 0 & 0 & \frac{\partial}{\partial z} \\ \frac{\partial}{\partial y} & \frac{\partial}{\partial x} & 0 \\ 0 & \frac{\partial}{\partial z} & \frac{\partial}{\partial y} \\ \frac{\partial}{\partial z} & \frac{\partial}{\partial x} & 0 \end{pmatrix} \begin{pmatrix} u \\ v \\ w \end{pmatrix} = [B]\boldsymbol{\phi}^{(e)} \tag{50}$$

were $[B]$ incorporates the matrix of shape functions $[N]$:

$$[B] = \begin{pmatrix} \frac{\partial}{\partial x} & 0 & 0 \\ 0 & \frac{\partial}{\partial y} & 0 \\ 0 & 0 & \frac{\partial}{\partial z} \\ \frac{\partial}{\partial y} & \frac{\partial}{\partial x} & 0 \\ 0 & \frac{\partial}{\partial z} & \frac{\partial}{\partial y} \\ \frac{\partial}{\partial z} & \frac{\partial}{\partial x} & 0 \end{pmatrix} [N] \tag{51}$$

Using this relation and the shape function approximation of the displacement functions $\mathbf{U}$ (see equation (47)), equation (49) can be stated as:

$$\pi_p^{(e)} = \frac{1}{2} \iiint\limits_{V^{(e)}} (\boldsymbol{\phi}^{(e)})^T [B]^T [D][B] \boldsymbol{\phi}^{(e)} dV$$

$$- \iiint\limits_{V^{(e)}} (\boldsymbol{\phi}^{(e)})^T [N]^T \boldsymbol{\psi}_b dV - \iint\limits_{S^{(e)}} (\boldsymbol{\phi}^{(e)})^T [N]^T \boldsymbol{\psi}_s dS \tag{52}$$

Since the vector of nodal displacements $\boldsymbol{\phi}^{(e)}$ is no function of the integration variable, it can be taken out of the integrals. This vector is associated with a specific element e. If the matrices inside the integral are appropriately enlarged with zeros, the element nodal displacement vectors can be gathered to a vector $\boldsymbol{\Phi}$, which contains all nodal displacements. This global nodal displacement vector has a dimension of 3M, were M is the number of nodes in the body. Based on this considerations the potential energy of the body is found as:

$$\pi_p = \frac{1}{2} \boldsymbol{\Phi}^T \sum_{e=1}^{N} \left[\iiint\limits_{V^{(e)}} [B]^T [D][B] dV \right] \boldsymbol{\Phi}$$

$$- \boldsymbol{\Phi}^T \sum_{e=1}^{N} \left[\iiint\limits_{V^{(e)}} [N]^T \boldsymbol{\psi}_b dV - \iint\limits_{S^{(e)}} [N]^T \boldsymbol{\psi}_s dS \right] \tag{53}$$

Since equation (53) expresses the potential energy in terms of the nodal displacements $\boldsymbol{\Phi}$, an extremum of the potential energy, which is generally associated with its minimum, can be found by requiring:

$$\frac{\partial \pi_p}{\partial \Phi_1} = \frac{\partial \pi_p}{\partial \Phi_2} = \ldots = \frac{\partial \pi_p}{\partial \Phi_{3M}} = 0 \tag{54}$$

This yields for equation (53):

$$\left[\sum_{e=1}^{N} \iiint_{V^{(e)}} [B]^T[D][B]dV\right]\boldsymbol{\Phi} =$$

$$= \sum_{e=1}^{N} \iiint_{V^{(e)}} [N]^T\boldsymbol{\psi}_b dV + \sum_{e=1}^{N} \iint_{S^{(e)}} [N]^T\boldsymbol{\psi}_s dS \tag{55}$$

This equation can be written as:

$$\sum_{e=1}^{N} [K^{(e)}]\boldsymbol{\Phi} = \sum_{e=1}^{N} \mathbf{P}_b^{(e)} + \mathbf{P}_s^{(e)} \tag{56}$$

or

$$[K]\boldsymbol{\Phi} = \mathbf{P} \tag{57}$$

Equation (57) represents a system of linear equation which after solution yields the nodal nodal displacements of the body $\boldsymbol{\Phi}$.

The different parts of equation (55), (56) and (57) are named:

$$[K^{(e)}] = \iiint_{V^{(e)}} [B]^T[D][B]dV \qquad \text{Element stiffness matrix}$$

$$[K] = \sum_{e=1}^{N} [K^{(e)}] \qquad \text{Global stiffness matrix}$$

$$\mathbf{P}_b^{(e)} = \iiint_{V^{(e)}} [N]^T\boldsymbol{\psi}_b dV \qquad \text{Vector of element body forces}$$

$$\mathbf{P}_s^{(e)} = \iint_{S^{(e)}} [N]^T\boldsymbol{\psi}_s dS \qquad \text{Vector of element surface forces}$$

$$\mathbf{P} = \sum_{e=1}^{N} \mathbf{P}_b^{(e)} + \mathbf{P}_s^{(e)} \qquad \text{Global force vector}$$

Central to this procedure is the assemblage of the matrices [B], which characterize element strains and the integrations over the element volumes to obtain the element stiffness matrix. As apparent from equation (51), a differentiation of the shape functions is required. In the case of a tetrahedron with linear approximation functions,

the matrix of shape functions can be written as:

$$[N] = \begin{bmatrix} N_i & 0 & 0 & N_j & 0 & 0 & N_k & 0 & 0 & N_l & 0 & 0 \\ 0 & N_i & 0 & 0 & N_j & 0 & 0 & N_k & 0 & 0 & N_l & 0 \\ 0 & 0 & N_i & 0 & 0 & N_j & 0 & 0 & N_k & 0 & 0 & N_l \end{bmatrix} \quad (58)$$

This represents the generalization of matrix (33) to a vector field variable. The shape functions are given by equation (34). Since the variables x,y and z appear linearly in them, only the coefficients of the shape functions appear in the matrix [B]:

$$[B] = \frac{1}{6V} \begin{pmatrix} b_i & 0 & 0 & b_j & 0 & 0 & b_k & 0 & 0 & b_l & 0 & 0 \\ 0 & c_i & 0 & 0 & c_j & 0 & 0 & c_k & 0 & 0 & c_l & 0 \\ 0 & 0 & d_i & 0 & 0 & d_j & 0 & 0 & d_k & 0 & 0 & d_l \\ c_i & b_i & 0 & c_j & b_j & 0 & c_k & b_k & 0 & c_l & b_l & 0 \\ 0 & d_i & c_i & 0 & d_j & c_j & 0 & d_k & c_k & 0 & d_l & c_l \\ d_i & 0 & b_i & d_j & 0 & b_j & d_k & 0 & b_k & d_l & 0 & b_l \end{pmatrix} \quad (59)$$

This results in the matrix product $[B]^T[D][B]$ becoming independent of the integral over the volume of the element. Thus the evaluation of the integral yields the volume of the tetrahedron element (30) and the element stiffness matrix becomes:

$$[K^{(e)}] = V^{(e)}[B]^T[D][B]$$

In the case of a quadratic hexahedron element, the creation of the element stiffness matrix is more complicated. Like for the tetrahedron it is based on the relation (51). The matrix of shape functions [N] is now of the dimension 3x60 with the shape functions defined by equation (36) to (39). While the derivatives of the relation (51) are in terms of the global coordinate system x, y and z, the shape functions have been expressed in the natural coordinate system r, s, and t of the hexahedron. To carry out these differentiations the chain rule is applied:

$$\begin{pmatrix} \frac{\partial N_i}{\partial r} \\ \frac{\partial N_i}{\partial s} \\ \frac{\partial N_i}{\partial t} \end{pmatrix} = \begin{pmatrix} \frac{\partial N_i}{\partial x}\frac{\partial x}{\partial r} + \frac{\partial N_i}{\partial y}\frac{\partial y}{\partial r} + \frac{\partial N_i}{\partial z}\frac{\partial z}{\partial r} \\ \frac{\partial N_i}{\partial x}\frac{\partial x}{\partial s} + \frac{\partial N_i}{\partial y}\frac{\partial y}{\partial s} + \frac{\partial N_i}{\partial z}\frac{\partial z}{\partial s} \\ \frac{\partial N_i}{\partial x}\frac{\partial x}{\partial t} + \frac{\partial N_i}{\partial y}\frac{\partial y}{\partial t} + \frac{\partial N_i}{\partial z}\frac{\partial z}{\partial t} \end{pmatrix} \quad (60)$$

$$= \begin{bmatrix} \frac{\partial x}{\partial r} & \frac{\partial y}{\partial r} & \frac{\partial z}{\partial r} \\ \frac{\partial x}{\partial s} & \frac{\partial y}{\partial s} & \frac{\partial z}{\partial s} \\ \frac{\partial x}{\partial t} & \frac{\partial y}{\partial t} & \frac{\partial z}{\partial t} \end{bmatrix} \begin{pmatrix} \frac{\partial N_i}{\partial x} \\ \frac{\partial N_i}{\partial y} \\ \frac{\partial N_i}{\partial z} \end{pmatrix} = [J] \begin{pmatrix} \frac{\partial N_i}{\partial x} \\ \frac{\partial N_i}{\partial y} \\ \frac{\partial N_i}{\partial z} \end{pmatrix} \quad (61)$$

The matrix [J] is the Jacobian, which can be written (using (35)) as:

$$[J] = \begin{bmatrix} \frac{\partial x}{\partial r} & \frac{\partial y}{\partial r} & \frac{\partial z}{\partial r} \\ \frac{\partial x}{\partial s} & \frac{\partial y}{\partial s} & \frac{\partial z}{\partial s} \\ \frac{\partial x}{\partial t} & \frac{\partial y}{\partial t} & \frac{\partial z}{\partial t} \end{bmatrix} = \begin{bmatrix} \sum\limits_{i=1}^{20} \left(\frac{\partial N_i}{\partial r} x_i \right) & \sum\limits_{i=1}^{20} \left(\frac{\partial N_i}{\partial r} y_i \right) & \sum\limits_{i=1}^{20} \left(\frac{\partial N_i}{\partial r} z_i \right) \\ \sum\limits_{i=1}^{20} \left(\frac{\partial N_i}{\partial s} x_i \right) & \sum\limits_{i=1}^{20} \left(\frac{\partial N_i}{\partial s} y_i \right) & \sum\limits_{i=1}^{20} \left(\frac{\partial N_i}{\partial s} z_i \right) \\ \sum\limits_{i=1}^{20} \left(\frac{\partial N_i}{\partial t} x_i \right) & \sum\limits_{i=1}^{20} \left(\frac{\partial N_i}{\partial t} y_i \right) & \sum\limits_{i=1}^{20} \left(\frac{\partial N_i}{\partial t} z_i \right) \end{bmatrix} \tag{62}$$

For small distortions of the element, the Jacobian matrix is invertible. This yields:

$$\left\{ \begin{array}{c} \frac{\partial N_i}{\partial x} \\ \frac{\partial N_i}{\partial y} \\ \frac{\partial N_i}{\partial z} \end{array} \right\} = [J]^{-1} \left\{ \begin{array}{c} \frac{\partial N_i}{\partial r} \\ \frac{\partial N_i}{\partial s} \\ \frac{\partial N_i}{\partial t} \end{array} \right\} \tag{63}$$

from which the derivatives with respect to x, y and z can be computed.

To obtain the element stiffness matrix, it is necessary to carry out the integral over the volume of the element. Unlike in the case of linear approximation functions, the integral depends on the variables r, s and t. Because of the transformation to natural coordinates, the stiffness matrix can be written as:

$$[K^{(e)}] = \int\limits_{-1}^{1} \int\limits_{-1}^{1} \int\limits_{-1}^{1} [B]^T[D][B] \; |J| \; dr \; ds \; dt \tag{64}$$

were $|J|$ represents the determinant of the transformation, which is the determinant of the Jacobian matrix. This integral is evaluated numerically. Several schemes like Newton-Cotes and Gaussian quadrature are used for this purpose. Two point Gaussian quadrature has proved to be an effective method, to solve equation (64). Unlike the Newton-Cotes scheme, Gaussian quadrature employs integration points which are unevenly spaced and will be denoted R_i, S_j and T_k.

Equation (64) then becomes:

$$[K^{(e)}] = \sum_{R_i=R_1}^{R_2} \sum_{S_j=S_1}^{S_2} \sum_{T_k=T_1}^{T_2} \left([B]^T[D][B] \; |J| \right)_{R_i, S_j, T_k} \tag{65}$$

The expression

$$\left([B]^T[D][B] \; |J| \right)_{R_i, S_j, T_k}$$

indicates that the summations in equation (65) are evaluated at the points R_i, S_j and T_k. For a cube with unit side length and two point Gaussian quadrature, these points are $R_1 = S_1 = T_1 = -0.57735$ and $R_2 = S_2 = T_2 = +0.57735$. This procedure needs to be carried out for every element and the global stiffness matrix is then assembled from the element stiffness matrices.

2.2.4 Derivation of the Finite Element Method - Dynamic Case

As in the static case, the derivation of the finite element method for a dynamic problem rests on a variational principle. Using Hamilton's principle, this can be stated as:

$$\delta \int_{t_1}^{t_2} L \, dt = 0 \tag{66}$$

Here L indicates the Lagrangian of the system, given by

$$L = T - \pi_p \tag{67}$$

were T is the kinetic and π_p the potential energy of the body.

By using the field variable $\dot{\mathbf{U}}$ of displacement-velocity and the element density ρ, the kinetic energy of an element e can be expressed as:

$$T^{(e)} = \frac{1}{2} \iiint_{V^{(e)}} \rho \left(\dot{\mathbf{U}}\right)^T \dot{\mathbf{U}} dV \tag{68}$$

The element potential energy of an element is given by (49). If the existence of a dissipative force proportional to the velocity is assumed, the dissipative function of the element can be defined as:

$$R^{(e)} = \frac{1}{2} \iiint_{V^{(e)}} \left(\dot{\mathbf{U}}\right)^T [\Pi] \dot{\mathbf{U}} dV \tag{69}$$

where $[\Pi]$ is the matrix of damping coefficients, analogously to $[D]$.

In the static case, the field variable $\mathbf{U}$ of displacement is expressed by nodal displacements, using shape functions:

$$\mathbf{U}(x, y, z, t) = [N(x, y, z)] \phi^{(e)}(t) \tag{70}$$

This transformation is also used in dynamic problems. Since the shape functions do not depend on time, they are extended here for the the field variable velocity as:

$$\dot{\mathbf{U}}(x, y, z, t) = [N(x, y, z)] \dot{\phi}^{(e)}(t) \tag{71}$$

The kinetic, potential and dissipative energies T, π_p and R can now be restated, using the relation (71). This yields for the kinetic energy:

$$T = \sum_{e=1}^{N} T^{(e)} = \frac{1}{2} \dot{\boldsymbol{\Phi}}^T \left[\sum_{e=1}^{N} \iiint_{V^{(e)}} \rho [N]^T [N] dV \right] \dot{\boldsymbol{\Phi}} \tag{72}$$

and for the potential energy analogously to (52):

$$\pi_p = \frac{1}{2} \boldsymbol{\Phi}^T \sum_{e=1}^{N} \left[\iiint_{V^{(e)}} [B]^T [D] [B] dV \right] \boldsymbol{\Phi}$$

$$- \boldsymbol{\Phi}^T \sum_{e=1}^{N} \left[\iiint_{V^{(e)}} [N]^T \psi_b dV - \iint_{S^{(e)}} [N]^T \psi_s dS \right] \tag{73}$$

and for the dissipative function:

$$R = \sum_{e=1}^{N} R^{(e)} = \frac{1}{2} \dot{\boldsymbol{\Phi}}^T \left[\sum_{e=1}^{N} \iiint_{V^{(e)}} \mu [N]^T [N] dV \right] \dot{\boldsymbol{\Phi}} \tag{74}$$

Here $\boldsymbol{\Phi}$ and $\dot{\boldsymbol{\Phi}}$ are the vectors of global nodal displacements and the global vector of nodal velocity respectively. If matrices and vectors, which involve the integrals are defined by:

$$[M] = \sum_{e=1}^{N} \iiint_{V^{(e)}} \rho [N]^T [N] dV \qquad \text{Global mass matrix}$$

$$[K] = \sum_{e=1}^{N} \iiint_{V^{(e)}} [B]^T [D] [B] dV \qquad \text{Global stiffness matrix}$$

$$[C] = \sum_{e=1}^{N} \iiint_{V^{(e)}} [N]^T [\Pi] [N] dV \qquad \text{Global damping matrix}$$

$$\mathbf{P}_s = \sum_{e=1}^{N} \iint_{S^{(e)}} [N]^T \psi_s dS \qquad \text{Vector of nodal surface forces}$$

$$\mathbf{P}_b = \iiint_{V^{(e)}} [N]^T \psi_b dV \qquad \text{Vector of nodal body forces}$$

$$\mathbf{P} = \mathbf{P}_s + \mathbf{P}_b \qquad \text{Global vector of nodal body loads}$$

kinetic, potential and dissipative energies can be stated as:

$$T = \frac{1}{2}\dot{\boldsymbol{\Phi}}^T[M]\dot{\boldsymbol{\Phi}}$$

$$\pi_p = \frac{1}{2}\boldsymbol{\Phi}^T[K]\boldsymbol{\Phi} - \boldsymbol{\Phi}^T\mathbf{P}$$

$$R = \frac{1}{2}\dot{\boldsymbol{\Phi}}^T[C]\dot{\boldsymbol{\Phi}}$$

Hamilton's principle is equivalent to Lagrange's equations, which can be stated as:

$$\frac{d}{dt}\left(\frac{\partial L}{\partial \dot{\phi}_i}\right) - \left(\frac{\partial L}{\partial \phi_i}\right) + \left(\frac{\partial R}{\partial \dot{\phi}_i}\right) = 0 \tag{75}$$

Here it is assumed that displacements are expressed in terms of the global vector of nodal displacements $\boldsymbol{\Phi}$. Derivatives in equation (75) are with respect to the components of this vector ϕ_i or its time-derivative $\dot{\phi}_i$ (i.e. the nodal velocity). The function R incorporates dissipative properties of the body. If the relations for the kinetic, potential and dissipative energies found above are put into equation (75), the equation of motion of the body can be obtained as:

$$[M]\ddot{\boldsymbol{\Phi}}(t) + [C]\dot{\boldsymbol{\Phi}}(t) + [K]\boldsymbol{\Phi}(t) = \mathbf{P}(t) \tag{76}$$

This matrix equation needs to be integrated over time to obtain the nodal movements of the body.

In most cases little is known about the damping properties of a elastic body. Because of this, equation (76) is often simplified by expressing the damping matrix as a linear combination of the mass and stiffness matrix (Rayleigh damping):

$$[C] = a_d[M] + b_d[K] \tag{77}$$

Here a_d and b_d are coefficients that determine to which degree mass and stiffness matrices participate in the damping matrix.

2.2.5 Time-Integration of Dynamic Problems

Several schemes exist to perform the time-integration of equation (76). Newmark's method and nodal superposition are two schemes that are commonly applied for this purpose.

Using Newmark's method, the desired time interval is broken down into successive time steps. The time intervals Δt of the steps need not have identical length though

there may be a upper bound to them. Body movements after the first time step are computed, starting from an initial configuration with respect to nodal displacements and velocities. The configuration at the end of this step then serves as initial condition for the next step. This procedure is repeated till the end of the desired time interval is reached. For each step, a solution to the equation:

$$[M]\ddot{\boldsymbol{\Phi}}^{(t+\Delta t)} + [C]\dot{\boldsymbol{\Phi}}^{(t+\Delta t)} + [K]\boldsymbol{\Phi}^{(t+\Delta t)} = \mathbf{P}^{(t+\Delta t)} \tag{78}$$

is sought, were the superscript $(t + \Delta t)$ indicates the value of a variable at the end of the next time step. Known at the actual time t are the nodal displacements, velocities and accelerations. Newmark suggested the following formulas to approximate displacements and velocities after a step Δt:

$$\dot{\boldsymbol{\Phi}}^{t+\Delta t} = \dot{\boldsymbol{\Phi}}^{t} + (1 - \gamma)\Delta t\ddot{\boldsymbol{\Phi}}^{t} + \gamma\Delta t\ddot{\boldsymbol{\Phi}}^{t+\Delta t} \tag{79}$$

$$\boldsymbol{\Phi}^{t+\Delta t} = \boldsymbol{\Phi}^{t} + \Delta t\dot{\boldsymbol{\Phi}}^{t} + \left(\frac{1}{2} - \beta\right)(\Delta t)^2\ddot{\boldsymbol{\Phi}}^{t} + \beta(\Delta t)^2\ddot{\boldsymbol{\Phi}}^{t+\Delta t} \tag{80}$$

Equation (80) can be inverted to express $\ddot{\boldsymbol{\Phi}}^{t+\Delta t}$ in terms of $\boldsymbol{\Phi}^{t+\Delta t}$. This formulation can than be used in equation (79) to replace $\ddot{\boldsymbol{\Phi}}^{t+\Delta t}$. The resulting expressions for the accelerations and velocities at the end of the time step only include the known variables $\ddot{\boldsymbol{\Phi}}^{t}$, $\dot{\boldsymbol{\Phi}}^{t}$, $\boldsymbol{\Phi}^{t}$ and the unknown nodal vector of displacements $\boldsymbol{\Phi}^{t+\Delta t}$. They are substituted into equation(78). This yields a system of equations for the unknown vector $\boldsymbol{\Phi}^{t+\Delta t}$, which can be solved using standard techniques like LU- or Cholesky-decomposition. After every step velocities and accelerations need to be updated using equation (80) and (79). The advantage of the Newmark method is its simplicity and unconditional stability if γ is chosen as $1/2$ (to avoid artificial damping) and β as $1/6$, which implies a linear variation of the acceleration in the time interval Δt. On the other hand the computational work involved in this method is proportional to the number of required time steps. This is prohibitive if the discretization of a body leads to a large number of elements. To overcome this limitation the mode superposition method can be applied.

The basic idea of the mode superposition method is to uncouple (i.e. diagonalize) equation (76) by a linear transformation. Using the initial conditions of the system, the uncoupled differential equations can be solved. The resulting generalized displacements are then transformed back. The transformation can be stated as:

$$\boldsymbol{\Phi}(t) = [T]\boldsymbol{\Theta}(t) \tag{81}$$

Since in general only two matrices can be diagonalized simultaneously, assumption (77) is used to bring equation (76) into a appropriate form. Substituting the transformation (81) into equation (76) yields:

$$[\underline{M}]\ddot{\boldsymbol{\Theta}}(t) + [\underline{C}]\dot{\boldsymbol{\Theta}}(t) + [\underline{K}]\boldsymbol{\Theta}(t) = \underline{\mathbf{P}}(t) \tag{82}$$

with

$$[\underline{M}] = [T]^T[M][T]$$
$$[\underline{C}] = [T]^T[C][T]$$
$$[\underline{K}] = [T]^T[K][T]$$
$$\underline{\mathbf{P}} = [T]^T\mathbf{P}$$

The transformation matrix $[T]$ can be found by considering the solutions to the undamped free vibrational equilibrium equation which corresponds to (82). It can be stated as:

$$[\underline{M}]\ddot{\Theta} + [\underline{K}]\Theta = \mathbf{0} \tag{83}$$

This equation can be solved by:

$$\Theta = \Xi \sin[\omega(t - t_0)] \tag{84}$$

After substitution of this solution into (83) a generalized eigenproblem is obtained:

$$\omega^2[\underline{M}]\Xi = [\underline{K}]\Xi \tag{85}$$

Using standard techniques, eigenvectors Ξ_i and eigenfrequencies ω_i with the properties

$$\Xi_i^T M \Xi_i = \begin{cases} 1 & \text{if i = j} \\ 0 & \text{if i} \neq \text{j} \end{cases}$$

and

$$0 \leq \omega_1^2 \leq \ldots \leq \omega_i^2 \leq \ldots$$

if found. The eigenvectors Ξ_i are termed mode shape vectors. After arranging them as columns of the modal matrix $[\Xi]$ and the eigenfrequencies in a diagonal matrix $[\Omega]^2$, the solutions of (85) can be written as:

$$[\underline{M}][\Xi][\Omega]^2 = [\underline{K}][\Xi] \tag{86}$$

Using this equation and the orthogonality relation $[\Xi]^T[\underline{M}][\Xi] = \mathbf{I}$ one finds

$$[\Xi]^T[\underline{K}][\Xi] = [\Omega]^2$$

Thus $[\Xi]$ would be a suitable transformation matrix $[T]$. With the help of this relations and assumption (77), equation (82) becomes:

$$\ddot{\Theta}(t) + (a_d\mathbf{I} + b_d[\Omega]^2)\dot{\Theta}(t) + [\Omega]^2\Theta(t) = \underline{\mathbf{P}}(t) \tag{87}$$

By taking the initial conditions of the body and (time-dependent) external forces into account, this set of decoupled differential equations can be solved numerically.

The main advantage of the node superposition method is that only a subset of the eigenfrequencies need to be considered if the external forces vary sufficiently smooth over time. In this case only a small number of the eigenvectors, which correspond to the lowest eigenfrequencies, are used in the transformation. Critically to this procedure is the choice of a sufficient number of eigenmodes. Compared to a time-stepping algorithm like Newmark's method, the modal superposition technique offers considerably reduced computational work if the requirement of smoothly varying external forces is met.

2.3   Transfer Function

The dynamic properties of a mechanical system can be described conveniently with *transfer functions* if the system possesses certain properties. Its underlying differential equation is required to be linear as well as time invariant. For an externally applied sinusoidal stimulus, such a system exhibits a sinusoidal response, with the amplitude and phase shift depending on the applied frequency. This approach is used here to describe the frequency dependent displacement amplitudes and phase shifts, relative to sinusoidal head accelerations.

For an infinitely extended, planar otolith, Grant et al. derived an analytical solution (Grant et al., 1993). They assumed a two-layered membrane: an otoconia and a gel layer, covered by endolymph fluid. Because of recent physiological findings, their approach was extended in this investigation to a three-layer system by including an intermediate mesh layer. The transfer function of this system was derived by taking the Laplace transforms of the individual parts and connecting them via boundary conditions. This yields a transfer function which describes the frequency dependence of the displacement amplitude at the gel/mesh layer boundary. This location was chosen because it is assumed that the displacements in this region are sensed by the hair cells and subsequently signaled to the brain. The transfer function represents a one-dimensional approximation of the displacement amplitudes. Displacements are strictly parallel to the the layers.

The dynamics of the otoconia layer in a lumped analysis can be described as:

$$\rho_o h_o \frac{\partial v_o}{\partial t} - (\rho_o - \rho)h_o B =$$

$$\mu_f \left[\frac{\partial v_f}{\partial y_f}\right]_{y_f=0} - G_m \int\limits_0^t dt \left[\frac{\partial v_m}{\partial y_m}\right]_{y_m=h_m} - \mu_m \left[\frac{\partial v_m}{\partial y_m}\right]_{y_m=h_m} \tag{88}$$

This differential equation is written with respect to the velocity v_o of the otoconia layer. Inertial and external forces are indicated on the left hand side of the equation.

These forces are equated to forces acting on the boundary with the endolymph fluid and the mesh layer (see Fig. 16). The velocities of the mesh and endolymph layer are indicated by v_m and v_f respectively. While the shear elasticity of the mesh layer is measured by the shear modulus G_m, it is assumed that the endolymph fluid is not capable of emanating forces proportional to static displacements. Forces on the otoconia layer due to the endolymph fluid are therefore viscous forces proportional to the velocity at the boundary of the layers. This essentially yields damping of the otoconia layer movements. Damping in addition with elastic forces are assumed at the mesh layer boundary. The shear viscosity of those layers are indicated by μ_m (mesh layer) and μ_f (endolymph fluid). Heights of the otoconia, mesh and gel layer are termed h_o, h_m and h_g respectively. The variables y_f, y_m and y_g indicate that they are valid only within their respective layers.
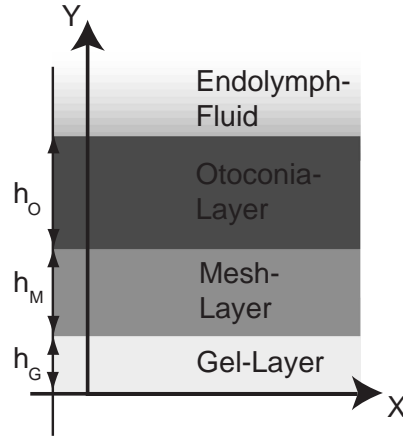
Figure 16: Geometrical variables and structure of the otolith membrane for the derivation of the mechanical transfer function.

B is an external acceleration of the body directed parallel to the layers and $\rho_o - \rho = \rho_{eff}$ the difference between the density of the otoconia layer and the surrounding material. The difference is called the effective density. It will be assumed that initially the velocity v_o and displacement δ_o of the otoconia layer is zero:

$$v_o(y, 0) = 0, \qquad \delta_o(y, 0) = 0$$

The dynamics of the mesh layer can be described by:

$$\rho \frac{\partial v_m}{\partial t} = G_m \int\limits_0^t dt \left[\frac{\partial^2 v_m}{\partial y_m^2} \right] + \mu_m \frac{\partial^2 v_m}{\partial y_m^2} \tag{89}$$

As in the case of the otoconia membrane, this is a partial differential equation for the velocity, here the velocity function within the mesh layer. Inertial forces are on

the left hand side of the equation while elastic and damping forces are on the right hand side. A similar equation can be stated for the gel layer:

$$\rho \frac{\partial v_g}{\partial t} = G_g \int\limits_0^t dt \left[\frac{\partial^2 v_g}{\partial y_g^2}\right] + \mu_g \frac{\partial^2 v_g}{\partial y_g^2} \tag{90}$$

The parameters in this partial differential equation with respect to the gel velocity v_g are the shear modulus G_g and the shear viscosity μ_g. Initial conditions for equation (89) and (89) are chosen in accordance with the otoconia layer conditions:

$$v_m(y_m, 0) = 0, \qquad \delta_m(y_m, 0) = 0$$

and

$$v_g(y_g, 0) = 0, \qquad \delta_g(y_g, 0) = 0$$

Mesh and gel layer differ with respect to their boundary conditions. At the boundary with the otoconia layer, the mesh layer velocity is equal to the otoconia layer velocity. Similarly the velocity at the gel/mesh layer interface v_{gm} is identical in both layers. This can be stated as:

$$v_m(h_m, t) = v_o(t), \qquad v_m(0, t) = v_{gm}(t)$$

Since the gel layer is tightly attached to the skull, the velocity is zero at this boundary. Further, the velocity at the mesh layer interface is required to match. Thus:

$$v_g(h_g, t) = v_{gm}(t), \qquad v_g(0, t) = 0$$

The mechanical properties of the endolymph fluid are described by:

$$\rho \frac{\partial v_f}{\partial t} = \mu_f \frac{\partial^2 v_f}{\partial y_f^2} \tag{91}$$

Based on the considerations regarding equation (88), only velocity related forces appear on the right hand side of the equation. Like in the other cases it is assumed that no movements are present at the otoconia- endolymph boundary initially:

$$v_f(0, 0) = 0$$

It is further assumed that no movement of the endolymph fluid occurs at large distances from the otoconia layer. Since the velocities at the otoconia/endolymph interface are required to match, the boundary conditions for the endolymph fluid can be stated as:

$$v_f(0, t) = v_o(t), \qquad v_f(\infty, t) = 0$$

Equation (88), (89), (90) and (91) are now subject to Laplace transforms with respect to time. This yields for the otoconia layer (taking the initial conditions into account):

$$\rho_o h_o s v_o(s) - h_o \rho_{eff} B = \left. \frac{\partial v_f}{\partial y_f} \right|_{y_f=0} - \frac{G_m}{s} \left. \frac{\partial v_m}{\partial y_m} \right|_{y_m=h_m} - \mu_m \left. \frac{\partial v_m}{\partial y_m} \right|_{y_m=h_m} \tag{92}$$

Here s indicates the Laplace transform variable. With the help of the initial conditions one obtains for the endolymph fluid:

$$\rho s v_f = \mu_f \frac{\partial^2 v_f}{\partial y_f^2}$$

which can also be stated as:

$$\frac{\partial^2 v_f}{\partial y_f^2} - \frac{\rho s}{\mu_f} v_f = 0 \tag{93}$$

Using $\sqrt{\rho s / \mu_f} = \kappa_f$ and the boundary conditions, this ordinary differential equation is solved by:

$$v_f(y_f, s) = v_o(s) e^{-y_f \kappa_f} \tag{94}$$

The derivative of this equation with respect to y_f, needed in (92), is then obtained as:

$$\frac{\partial v_f}{\partial y_f} = v_o \kappa_f e^{-y_f \kappa_f}$$

which evaluated at $y_f = 0$ yields:

$$\left. \frac{\partial v_f}{\partial y_f} \right|_{y_f=0} = v_o \kappa_f \tag{95}$$

By taking the Laplace transform of the mesh layer equation and using the initial conditions, one gets:

$$\rho s v_m = \frac{G_m}{s} \frac{\partial^2 v_m}{\partial y_m^2} + \mu_m \frac{\partial^2 v_m}{\partial y_m^2}$$

or

$$\frac{\partial^2 v_m}{\partial y_m^2} - \frac{\rho s^2}{G_m + \mu_m s} v_m = 0 \tag{96}$$

Using the boundary conditions, the solution to this differential equation can be stated as:

$$v_m(y_m, s) = \frac{v_{gm}(s)}{e^{-\kappa_m h_m} - e^{\kappa_m h_m}} \left[e^{-\kappa_m(h_m - y_m)} - e^{\kappa_m(h_m - y_m)} \right]$$
$$+ \frac{v_o(s)}{e^{-\kappa_m h_m} - e^{\kappa_m h_m}} \left[e^{-\kappa_m y_m} - e^{\kappa_m y_m} \right] \tag{97}$$

This equation employs the abbreviation:

$$\kappa_m = \sqrt{\frac{\rho s^2}{G_m + \mu_m s}}$$

From this, the derivatives of the velocity at the gel/mesh layer boundary can be derived as:

$$\left.\frac{\partial v_m}{\partial y_m}\right|_0 = \frac{v_o \kappa_m}{\sinh(\kappa_m h_m)} - v_{gm} \kappa_m \coth(\kappa_m h_m) \tag{98}$$

and at the mesh/otoconia layer interface:

$$\left.\frac{\partial v_m}{\partial y_m}\right|_{h_m} = -\frac{v_{gm} \kappa_m}{\sinh(\kappa_m h_m)} + v_o \kappa_m \coth(\kappa_m h_m) \tag{99}$$

Since the underlying partial differential equations of the gel and mesh layer are identical, the differential equation (96) after Laplace transformation is identical too. Using the boundary conditions, the solution for the gel layer can be stated as:

$$v_g(y_g, s) = v_{gm}(s) \frac{\sinh(\kappa_g y_g)}{\sinh(\kappa_g h_g)} \tag{100}$$

were the abbreviation

$$\kappa_g = \sqrt{\frac{\rho s^2}{G_g + \mu_g s}}$$

has been used. The derivative at the gel/mesh layer interface then becomes:

$$\left.\frac{\partial v_g}{\partial y_g}\right|_{h_g} = v_{gm} \kappa_g \frac{\cosh(\kappa_g h_g)}{\sinh(\kappa_g h_g)} = v_{gm} \kappa_g \coth(\kappa_g h_g) \tag{101}$$

The equations (92), (95), (98), (99) and 101 are five equations for the five unknowns:

$$v_o; \quad v_{gm}; \quad \left.\frac{\partial v_f}{\partial y_f}\right|_{y_f=0}; \quad \left.\frac{\partial v_m}{\partial y_m}\right|_{y_m=h_m}; \quad \left.\frac{\partial v_m}{\partial y_m}\right|_{y_m=0}$$

This system of equations can be solved for the velocity at the gel/mesh layer interface $v_{gm}(s)$. After some algebraic transformations the following result is obtained:

$$v_{gm}(s) = \frac{h_o \rho_{eff} B}{(\rho_o h_o s - \mu_f \kappa_f)\gamma_1 + (\frac{G_m}{s} + \mu_m)\gamma_2} \tag{102}$$

with

$$\gamma_1 = \frac{\kappa_m}{\kappa_g} \coth(\kappa_g h_g) \sinh(\kappa_m h_m) + \cosh(\kappa_m h_m)$$

and

$$\gamma_2 = -\frac{\kappa_m}{\sinh(\kappa_m h_m)} + \gamma_1 \kappa_m \coth(\kappa_m h_m)$$

Since the time integral of the velocity is the displacement, Laplace transformation and the assumption of no initial displacement produces:

$$\delta_{gm}(s) = \frac{1}{s} v_{gm}$$

After insertion of this result into equation (102) and dividing by B, the mechanical transfer function of the displacement at the gel/mesh layer boundary becomes:

$$\frac{\delta_{gm}}{B} = \frac{h_o \rho_{eff}}{(\rho_o h_o s - \mu_f \kappa_f) s \gamma_1 + (G_m + \mu_m s) \gamma_2} \tag{103}$$

The results can be visualized in the form of Bode plots which depict the amplitude and phase shift as a function of the stimulus frequency.

2.4 Fractional Calculus

The velocity of a particle is represented by the first derivative of its location with respect to time. Likewise acceleration corresponds to the second derivative. Fractional calculus generalizes this concept to differentiations of non-integer order. It is thus possible to define a 1.5 differentiation, with the resulting function being a "mixture" of velocity and acceleration. Fractional calculus is a general concept, which for example is applied to stimulus induced neural responses. It has been shown that the time-dependent, tonic/phasic excitation properties of neurons innervating the striola region can be described by this method (Hess, 1992).

Based on the mechanical displacement of the gel layer and polarization vector of striola hair cells, we calculated their static excitation at all time steps. Since the directions of the polarization vectors were manually adjusted under visual control, discontinuities were associated with the orientation of these directions. To reduce this local effect as well as numerical inaccuracies, we applied a simple moving average filter on neighboring striola points to smooth the local hair cell potential (Equation 106). This time series was then subjected to fractional differentiation. We used a fraction of $\varepsilon = 0.31$ (Hess, 1992). The differentiation was accomplished numerically using the Grünwald-Letnikov formula (Oldham and Spanier, 1974):

$$\frac{d^\varepsilon f(t)}{dt^\varepsilon} = \frac{1}{h^\varepsilon} \sum_{j=0}^{N} (-1)^j \frac{\Gamma(\varepsilon + 1)}{\Gamma(j + 1)\Gamma(\epsilon - j + 1)} f(t - jh) \tag{104}$$

Here h indicates the time step size, and Γ the gamma function. Subject to the fractional differentiation is the function f, (in our case the time series of excitations) which is given at discrete points in time. The sum needs to be evaluated for every time step. We varied the number of terms N, which participate in the sum, to test if convergence occurred. The Grünwald-Letnikov formula represents a generalization of the finite difference method to a non-integer order of differentiation.

3 Mechanical Results

3.1 Mechanical Properties of the Otolith Membrane

To characterize the mechanical system, we need to define the orientation of the otolith maculae and find reasonable estimates for its mechanical parameters. For the representation of spatial properties, the head centered stereotactic coordinate system was chosen. This is defined by the mid-sagittal plane and by Reid's plane (given by the lower rim of the orbita, and the center of the external acoustic meatus), with the positive x-, y-, and z-axis pointing forward, left, and upward, respectively. The otoconia-layer was assumed to have a constant height of 15μm while the height of the gel- and mesh-layer were taken to be 10μm (Grant and Cotton, 1990; Grant et al., 1993).

Gel-layer and otolith membrane density have been measured to be 1.0g/cm^3 (Money et al., 1971) while the mean density of the otoconia-layer is about 2.0g/cm^3 (Trincker, 1962). We chose to treat all layers as homogenous isotropic materials. The force-displacement relations of the gel-, mesh- and otoconia-layer are described by the Lamé constants λ_{gel}, μ_{gel}, λ_{mes}, μ_{mes} and λ_{oto} , μ_{oto} respectively. By assuming that the gel-layer is almost incompressible (Poisson constant $\nu = 0.49$) it is possible to obtain λ_{gel}. Young's modulus of the gel-layer E_{gel} was estimated to be 10.0 Pa (Kondrachuk, 2001a). This leads to a value for λ_{gel} of 164.4 Pa, and translates to a shear constant μ_{gel} of 3.35 Pa (Equation 13,14). This value is in good agreement with values derived from studies of human sensitivity to acceleration, which was measured to be 0.002g (Peters, 1969). Using the given material parameters, this acceleration leads to a deflection of the order of 1nm. Deflection measurements at the cochlea showed that this is the minimum magnitude the hair cells can detect (Sellick et al., 1982). Measurements of gel-layer elasticity of the bullfrog saccule lead to a Young's modulus E that was substantially larger, i.e. to a much stiffer gel-layer (Benser et al., 1993; Kondrachuk, 2000). This is probably due to the fact that the function of the frog saccule differs from that of the mammal saccule (Kondrachuk, 2000). Nevertheless, we used the elasticity ratio between gel-layer and mesh-layer ($E_{mes}/E_{gel} \approx 20$) found in that investigation to fix the elasticity of the mesh-layer and the otoconia-layer. We also assumed that these layers are virtually incompressible, like the gel-layer.

The damping effects are measured by the viscosity parameter. Based on electrophysiological studies (Goldberg et al., 1990a) it has been found that the shear viscosity of the gel layer is in the range between 0.1 Poise (Grant et al., 1993) and 1.0 Poise (Kondrachuk, 2000). We used a gel layer viscosity of 0.3 Poise. As mentioned before, stiffness-proportional Rayleigh damping was employed. To account for a viscosity of 0.3 Poise, the parameter b_d (see equation 77) was found to be 0.01 s. We

used the same value (b_d=0.01 s) to model the mesh layer, since this value has not been measured and the effects of damping should be small in this layer. We did not include damping in the otoconia layer because its structure differs from the other two layers. The remaining viscosity of the endolymph fluid has been measured to be 8.5 10^{-3} Poise (Steer, 1967).

The mechanical parameters used in this investigation are summarized in table 1.

	ρ [g/cm^3]	E [g/cm s^2]	ν [$-$]	*Viscosity* [g/cm s]
Endolymph fluid	1.0	-	-	$8.5 \cdot 10^{-3}$
Otoconia layer	2.0	$2.0 \cdot 10^3$	0.49	-
Mesh layer	1.0	$2.0 \cdot 10^3$	0.49	6.0
Gel layer	1.0	$1.0 \cdot 10^2$	0.49	0.3

Table 1: Mechanical parameters of the otolith membrane. Note that the viscosity parameter refers to shear displacements.

3.2 Static Results

3.2.1 Displacement Curves

For accelerations in the yaw, pitch, and roll plane we calculated the translation of one point at the gel/mesh-layer boundary. This location within the otolith membrane was selected because it is assumed that hair cell potential is sensitive to displacements at this boundary. The point was chosen in the central (striola) region to minimize possible effects of the otolith membrane lateral boundary. It is indicated by the black dot in Fig. 17.

Within each plane, all directions of acceleration were calculated, in steps of 30°. Fig. 18 shows the resulting displacements for the left utricle, and Fig. 19 the corresponding curves for the left saccule. It was possible to reproduce the curves with appropriately shifted and scaled sinusoidal functions to a high degree of precision. Note that even purely horizontal accelerations can induce a significant vertical displacement (Fig. 18A). Similarly, for purely vertical accelerations along the z-axis (i.e. up or down), the utricle mesh- and otoconia-layers are displaced significantly along the x-axis (Fig. 18B, 0°/180°). Since the otolith maculae are curved structures, this displacement is not constant throughout the maculae, i.e. different parts are displaced with different magnitudes and directions.
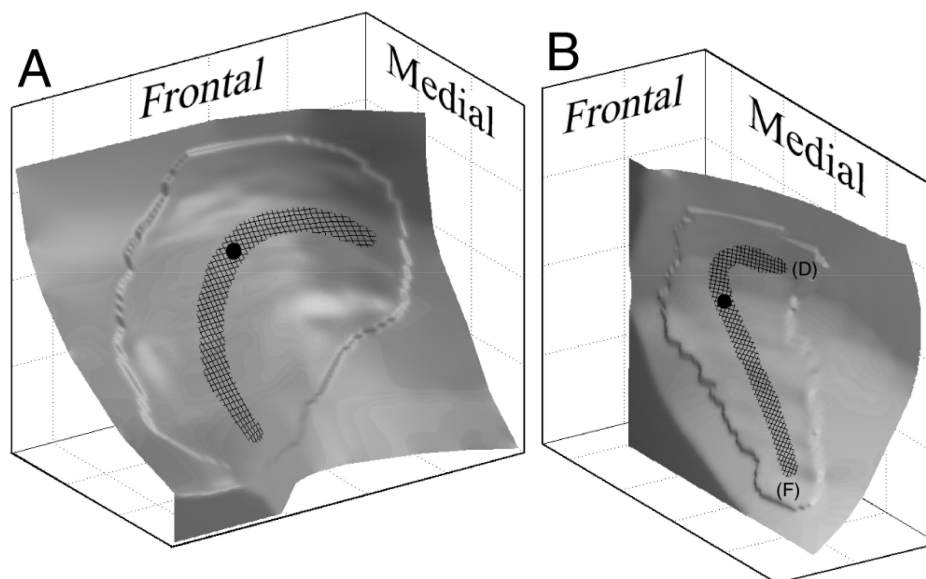
Figure 17: Location of points where displacements and hair cell activation were calculated. The positions are indicated by black dots. The letters (F) and (D) refer to Fig. 20.

3.2.2 Lateral Boundary of the Otolith Membrane

The simulation also allowed to study the effect of the lateral gel-layer extension on the displacement of the otolith membrane. Since the gel is clear it is hard to determine this parameter experimentally. A gel-layer that extends beyond the area covered by the otoconia membrane would need extra energy to deform. Thereby the exact magnitude of this effect depends on the area covered by the gel. To test the magnitude of that effect, the displacements of a gel-layer that has exactly the same size as the otoconia-layer (i. e. no extension) were calculated, and compared it with displacements of an otolith membrane with a large lateral extension of the underlying gel area.

Figure 18: 3D utricular displacements at the point indicated in Fig. 17A. The pictures on the left indicate the force directions. The x-axis points forward, the y-axis to the left, and the z-axis upward.

This extension was chosen so large that virtually no displacement occurred at the lateral gel-layer boundary. The results indicate that the lateral boundary of the gel-layer has only small effects that are confined to the vicinity of the lateral border.
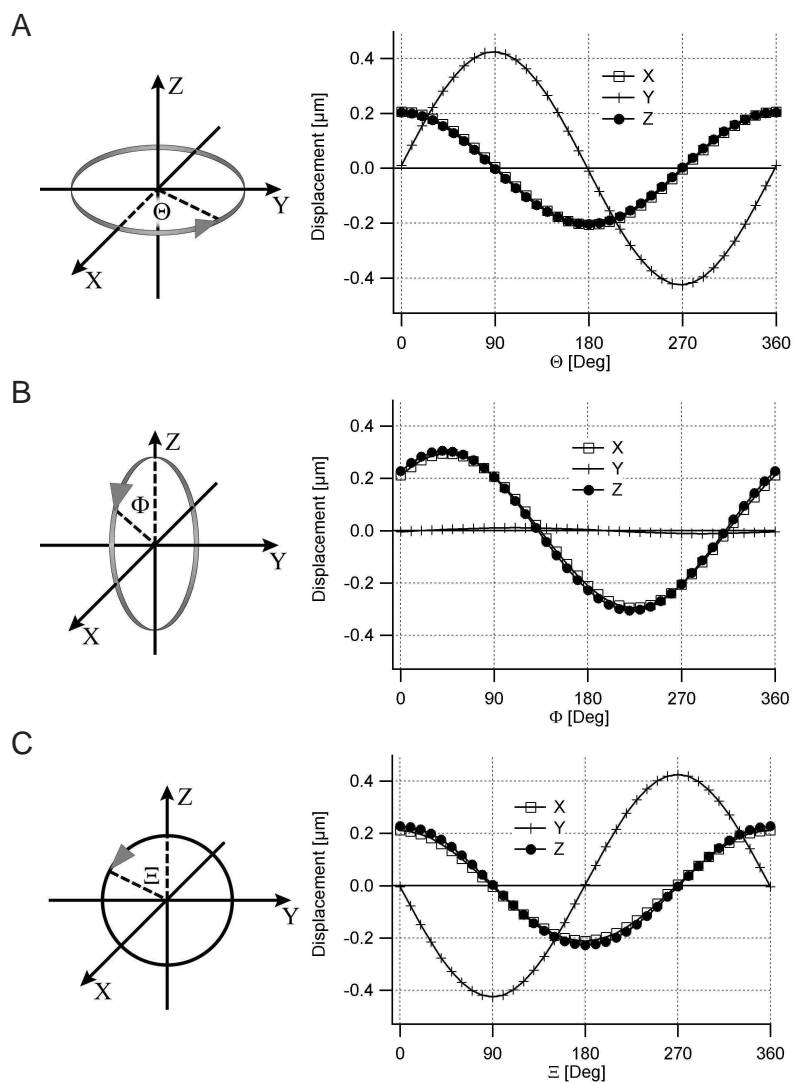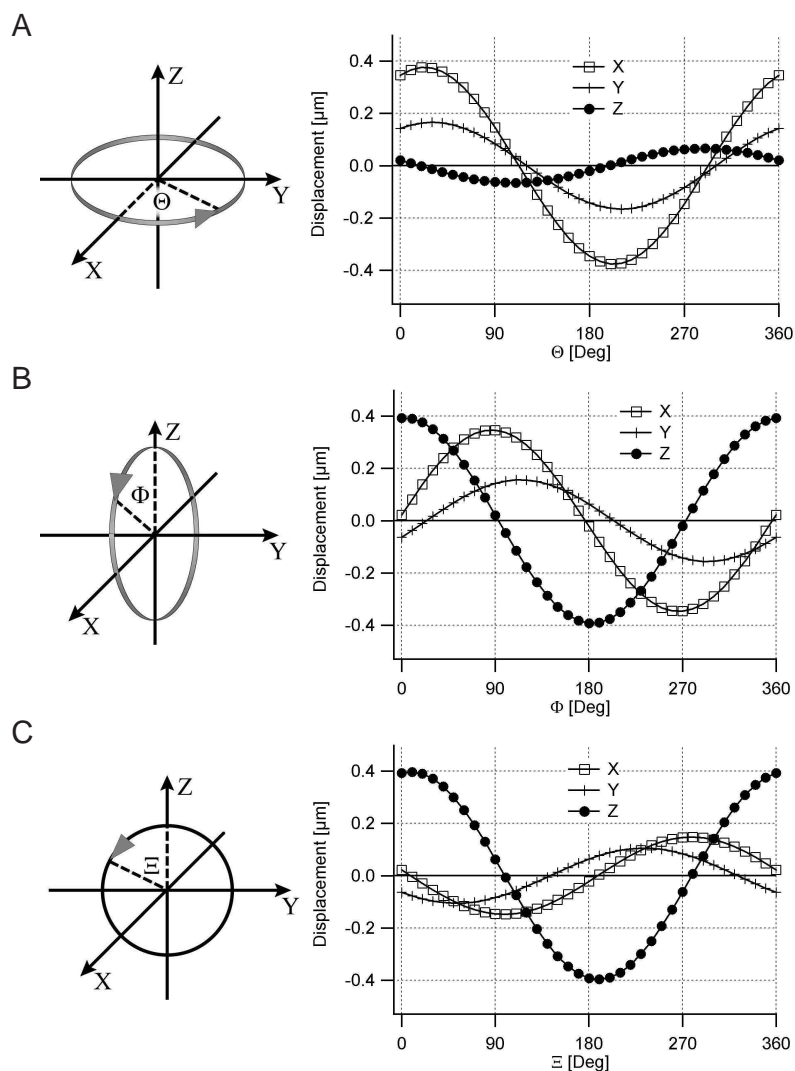
Figure 19: 3D saccular displacements at the point indicated in Fig. 17A. The pictures on the left indicate the force directions. The x-axis points forward, the y-axis to the left, and the z-axis upward.

3.2.3   Parameter Studies

For any numerical model of a biological system, the mechanical parameters that characterize the model can only be specified with a limited accuracy. One of the best established mechanical parameters of the otolith system is probably the effective density of the otoconia-layer. It is estimated that this value is correct within a range of 20%. It enters linearly into the model, which means that an error of the effective

density will lead to a proportional change of displacements. Similarly, an error in the height of the otoconia-layer causes a change of the perceived acceleration and affects the displacements linearly. We assume that the height of the otoconia-layer, like the height of all other layers, is associated with a maximum error of about 30%. A similar magnitude of the error probably exists for Young's modulus of the gel-layer. All these errors cause a proportional change of scale of the displacement axis in Figures 18 and 19, but do not affect other properties of the figures (sinusoidal shape, relative amplitudes, phase shifts).
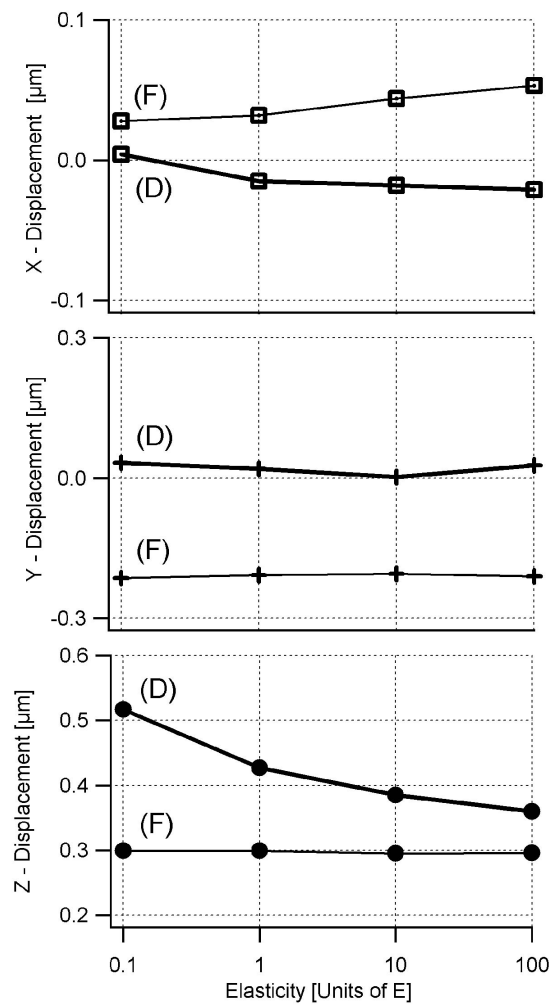
Figure 20: Dependence of deflection on the elasticity (Young's modulus) of the mesh- and otoconia-layer. The elasticity on the abscissa is in units of the elasticity used in the simulation. The x, y, and z-deflections at the points (F) and (D) of Fig. 17 correspond to a linear acceleration along the positive z-axis (e.g. head in upside-down position, $\Phi = 0°$ in Fig. 19.

Probably the least known mechanical parameters of mammal otoliths are the elasticity of the mesh- and the otoconia-layer. At least the parameters should be considerably larger than the elasticity of the gel-layer, since their filament matrix is much tighter connected. They determine how much distant parts of the otoliths interact.

As mentioned above, different parts of the otolith membrane, especially parts with clearly different orientations, interact only weakly if Young's modulus of mesh- and otoconia-layer is chosen twenty-fold larger than for the gel-layer. Figure 20 summarizes the effects on displacements of two points on the saccule membrane at the gel-/mesh-layer boundary if this parameter is changed. Note that the scaling is different for each direction of movement. The x-axis represents Young's modulus of elasticity in units chosen for our simulation (i. e. 1.0 represents 200.0 Pa). Each curve represents the displacement of a point on the saccule in the head down position ($\Phi = 0°$; Fig. 19). The curves labelled with "D" or F" represent the displacement of the corresponding points in Fig. 17. The displacements found at these points indicate the range of deflections of the membrane, since they were chosen in regions where the local slopes of the macula differed the most. All other displacements found on the saccule are somewhere between these curves. It can be seen that movements in the z-direction are affected strongest by a change of elasticity. Displacements at the point (F), which lies in a region that is comparatively flat, remain almost unaffected. In contrast, deflections at point (D) are markedly reduced. This is caused by the larger curvature of the otolith membrane in this region, which leads an additional bending of the mesh- and otoconia-layer compared to flat areas, where only shearing displacements in the gel-layer are observed. Similar effects would be observed if the elasticity of the gel-layer were changed. This effect is not considered here, since mesh- and otoconia-layer dominate the distribution of forces within the otolith membrane. With respect to parameter sensitivity we found that a wrong elasticity of the upper two layers cause changing deflections in regions with substantial curvature.

3.2.4   Curvature Effects

To investigate the effect of the otolith curvature in more detail, it is convenient to define a planar otolith with an orientation that locally resembles the curved maculae of real otoliths. Since otolith membranes are mainly flat structures, a plane is a reasonable local approximation of their shape. We defined planes by the linear equation:

$$z = ax + by \tag{105}$$

with x, y, and z indicating head coordinates, and a and b defining the orientation of the plane. The deflection of a planar otolith structure can be determined with a high degree of precision from a finite difference model (Grant and Cotton, 1990). Since a

planar structure is insensitive to acceleration components perpendicular to the plane, its displacement due to acceleration can be derived by projecting the acceleration into that plane. By comparing the response of such planar structures to the actual displacements as predicted by our 3D model, we numerically determined the plane orientation that best resembled the response of curved maculae for accelerations in the three head planes. We found that planar approximations show almost the same displacements as curved otolith membranes if the slope of the ideal plane corresponds to the local slope of the curved macula. To test this further we employed the model of a planar otolith macula with only the density of one single otoconia finite element being larger than the endolymph density. This approach is similar to the one used by Kondrachuk (Kondrachuk, 2000), with the difference that he considered local forces originating from the tip of a probe. Our approach led to local displacements around that element with an extension similar to the range where substantial changes of the macula curvature occur ($\sim 300 \mu$m). Only comparatively small displacements were found in elements that were further away from the otoconia element with a nonzero effective density.

3.2.5 Discussion of Static Mechanical Effects

Simulation of displacements of otolith membranes with numerical techniques has a long tradition. Early simulations were restricted by the limited anatomical knowledge about the otolith structure. Twizell (Twizell and Curran, 1977) and Hudetz (Hudetz, 1973) used a planar, two dimensional approximation of the otolith membrane with a space fixed lateral boundary. A marked improvement in our understanding of otolith mechanics was the introduction of a layered membrane structure (Grant et al., 1984; Grant and Best, 1986, 1987; Grant and Cotton, 1990; Grant et al., 1993). Grant was also the first to use the mechanics of visco-elastic materials to describe membrane dynamics. His approach allowed the investigation of static and dynamic responses, always making the assumption that the otolith epithelia can be approximated reasonably well by planar surfaces. The same assumption was made by Kondrachuk (Kondrachuk, 2000), who took up a suggestion by Kachar et al. (Kachar et al., 1990) and sub-divided the space between the macula and the otoconia-layer into two mechanically distinct parts. This allowed him to analyze the experimental findings by Benser et al. (Benser et al., 1993), and to determine the elastic properties of those layers. To our knowledge the simulations presented above are the first to consider the actual 3D structure of the otoliths. Our results suggest that the curvature of otolith membranes has no effect on the displacement of the membrane as a whole, and that distant parts of the membrane can act almost independently. The deflection is related to the local orientation of the macula, which can be approximated by a plane. Critical to this observation is the elasticity of

the mesh- and otoconia-layer. If the elasticity were smaller, parts of the membrane with different orientation would interact through forces transmitted by the upper layers. If the elasticity were higher, it might become necessary to take the local inhomogeneity of the membrane into consideration (for example the distribution of otoconia, which have a size of about 10μ m). Based on the parameters chosen for this investigation we speculate that the otolith membrane has evolved in a way that ensures non-interaction of parts with different orientations, while keeping the elasticity of the upper layers large enough to obtain a homogenous distribution of otoconia forces. We conclude that the curvature of the otolith maculae is directly related to the need to sense a particular aspect of the acceleration. It is not involved in some kind of mechanical "computation".

We found that the displacements of the otolith membrane due to static accelerations could be reproduced very well with sinusoidal functions. Since the partial differential equation that guides the displacement is linear and distant parts of the membrane do not interact, the mechanical response is determined by the local orientation of the macula. As the direction of the acceleration vector rotates, the displacements are largest if the vector is parallel to the local orientation of the macula, and zero if it is perpendicular to it. For angles between these extremes the displacements can be well approximated by sinusoidal functions since the displacements correspond to the projection of the acceleration vector into the local plane.

Numerical simulations of the macula organs are hampered by the lack of exact material parameters. For this reason we carefully evaluated the effects that would result from changes in the critical parameters. We found that, with the exception of the elasticity of the mesh- and otoconia-layer, all parameters just affect the magnitude of the displacement of the curves shown in Figures 18 and 19, while other properties of the curves are not altered. Given a gel-layer height of 10μ m, the predicted displacements on the order of several hundred nanometer seem reasonable for acceleration with 1g. Higher accelerations arise in daily life during running or jumping and the system should not be driven into saturation by these conditions. Of all the mechanical parameters the elasticity of the mesh and otoconia-layer is probably the least known, especially for mammal otoliths. Our investigations revealed that a change of this parameter leads to altered deflections of the otolith membrane, depending on the local curvature of the macula. For a better understanding of otolith kinematics it is necessary to experimentally determine these parameters more exactly.

Planar approximations of otolith structure are also used in models that try to determine the otolith contribution to eye movements (Merfeld et al., 1993; Glasauer and Merfeld, 1997; Haslwanter et al., 2000) or to the perceived orientation in space (Dai et al., 1989). These models generally assume that otoliths are perfect transducers of head accelerations. Our model does not directly contradict this assumption, especially since the simulations demonstrate that deflections occur regardless of the

direction of acceleration, i.e. that there are no "blind spots". Nevertheless, given the ambiguity of linear accelerations (they can be due to gravity, or due to real accelerations), it is questionable if the brain is able to interpret all acceleration signals correctly. It is likely that accelerations that are highly relevant in the usual scheme of head movements are detected more accurately. Variable stereocilia elasticity may be a way to tune mechanical responses. These hair bundles provide a substantial part of gel-layer elasticity, and it was found that their mechanical properties exhibit some variability (Benser et al., 1993). A systematic distribution of stereocilia elasticity over the macula may be able to guide deflections in a way optimized to species-specific needs.

3.3   Dynamic Results

While the knowledge about orientation with respect to gravity is of great significance for body posture, it is even more important for humans to detect changes of the orientation. Changes of the orientation with respect to gravity and changes of acceleration in general provide essential information for the control of a inherently unstable body.

3.3.1   Curvature Effects

Due to weak mechanical coupling, distant parts of the otolith structure interact only marginally (Jaeger et al., 2002). We therefore studied the dynamic effects of otolith curvature by investigating a comparatively small, quadratic section of the otolith (300μm x 300μm). The planar otolith section was deformed in such a way that the curved otolith region represented a section of a sphere with radius R (Fig. 21). A planar surface would correspond to an infinitely large curvature radius. The deformed structure was then oscillated sinusoidally, parallel to the tangent of the layers in the central region of the section, with a maximum acceleration of 1g, and a frequency between 0.1 and 10 Hz. This frequency range covers all typical head movements (Viirre and Demer, 1997). Due to the assumed incompressibility of the otolith membrane, accelerations perpendicular to the layers yield virtually no effect. Fig. 21 shows the transfer functions of the analytical solution (Equation 103), the planar and deformed otolith sections. It depicts the magnitude and phase of the displacements at the gel/mesh layer boundary in the central region of the section.
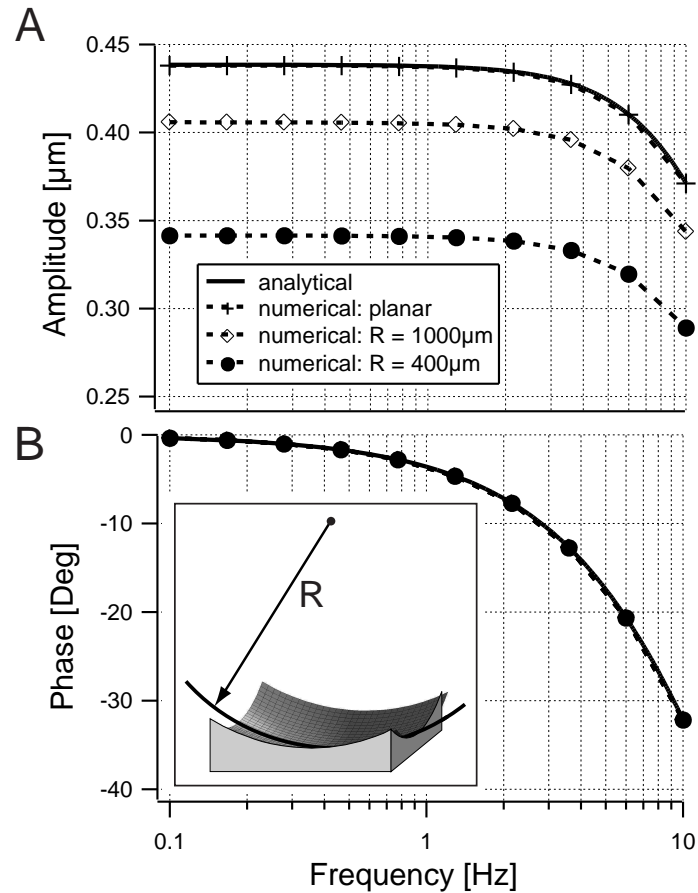
Figure 21: Transfer function of a quadratic otolith section at the gel/mesh layer boundary. A) While the displacements are identical for the planar section and the analytical case, finite curvature of the section leads to a reduction of the displacement. B) The phase shifts are unaltered by the magnitude of the curvature radius R. The inset illustrates the meaning of this parameter.

In all cases the phase shift is identical. The uppermost trace represents the amplitude of the planar sample, which coincides almost perfectly with the analytical solution. The lower traces indicate that for decreasing curvatures the displacement amplitude is progressively reduced. Figure 22A shows the relation between the displacement amplitude and curvature radius. While for a radius above 1000μm the amplitude reduction is <10% compared to the planar sample, it is becoming more pronounced for smaller radii. We found in our data set that the radius of curvature is in most areas larger than 1000μm. However, a small region on the utricle, which is marked on Fig. 22B as "large curvature area" (LC), shows a local curvature radius of only about 400μm.
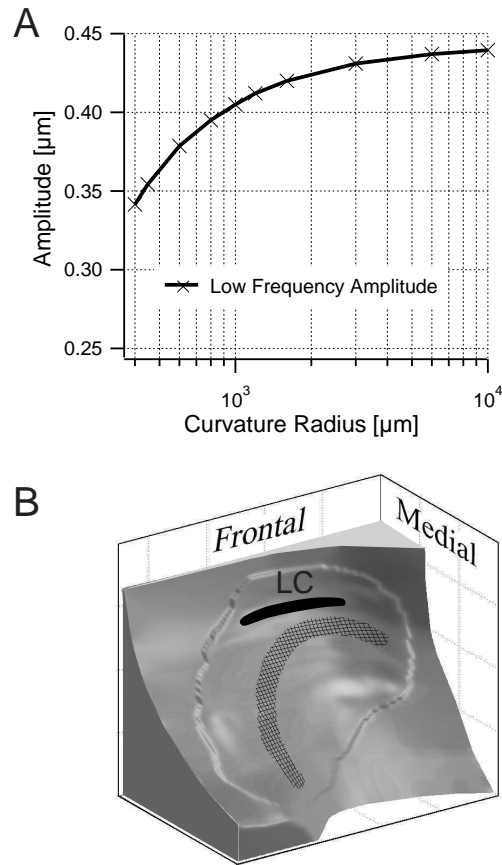
Figure 22: : A) Dependence of the displacement amplitude at low frequencies on the curvature radius. B) Region on the utricle where large curvature (LC) can be found. Large curvature corresponds to a small curvature radius.

3.3.2 Discussion of Dynamical Curvature Effects

Only few studies exist that have investigated the dynamic behavior of the otolith membrane (Grant and Cotton, 1990; Grant et al., 1993; Kondrachuk, 2001*b*). These studies were based on a number of simplifying assumptions: they assumed that the otolith membrane consists of two individual sub-layers with different mechanical properties and is planar. The present study eliminated these assumptions. In accordance with experimental findings (Kachar et al., 1990), we subdivided the otolith membrane into three different layer, i.e. we added a stiff intermediate mesh layer to the otolith structure. Both the finite element response and analytical transfer function that we derived for this setup showed that for flat parts of the otoliths, the mesh layer adds no new aspects at the gel/mesh layer boundary: The displacement amplitude remains constant for frequencies up to 1 Hz and decreases to zero for

higher frequencies, while the phase shift gradually increases. The numerically and the analytically derived transfer functions differ with respect to the treatment of the endolymph fluid: While the analytical solution incorporates velocity dependent forces of the endolymph on the otolith membrane, the finite element approach does not. The similarity in the predicted responses suggests that viscous forces from the endolymph have only minor effects on otolith displacements in the typical frequency range of head movements.

For the 3-dimensional shape of the otoliths, we used experimentally measured data from human otoliths (Takagi and Sando, 1988; Sato et al., 1992). Static investigations of otolith displacements that were based on these data have shown that the local displacements are largely determined by the local orientation of the otolith membrane (Jaeger et al., 2002). This allowed us to study the effects of curvature on otolith displacements on a small, quadratic slice. Our results indicate that curvature changes the response properties. While the phase shift remains identical to the planar case, the amplitude is reduced over the whole frequency range. This can be explained by the fact that elements outside the central region of the quadratic slice are not subject to the optimal, parallel acceleration. Instead their displacement depends on the local orientation. Since the deflections in the neighboring parts are smaller, the displacement in the central region is reduced too. This reduction increases as the radius of curvature becomes smaller. For most areas of the human otoliths the curvature radius is $>1000\mu$m, and the decrease of amplitude is less than 10%. However, on the utricle we also found a region where the radius is substantially smaller (Fig. 22B). Interestingly, this region of large curvature is close to the striola and shows a similar orientation. Speculations about the implications of this proximity become even more tempting by the fact that other researchers have put the striola more frontally and laterally than Lindeman did (Flock, 1964). It may be possible that the areas of large curvature are specifically used to somehow optimize the transduction of orientation and movement, especially since the direction of largest curvature and the direction of hair cell polarization coincide there.

3.3.3   Effects at Higher Frequencies

To study the effects of higher oscillation frequencies on the otolith membrane, we needed to abandon the simplifying assumption of isotropy in the *otoconia layer.* If there are deflections of the otolith structure, they should be found in the vicinity of the otoconia, since at least the gel layer is strongly damped. To investigate such effects, we constructed a simple model, which included otoconia separated by an isotropic inter-otoconial filament matrix. For this matrix we took a density of 1g/cm^3, and for the otoconia crystals a density of 2.7g/cm^3 (Money et al., 1971). Since measurements of the density of the otoconia layer, i.e. otoconia plus intercon-

necting matrix, have shown that the combined density is about 2g/cm^3 (Trincker, 1962), we chose the distance between the otoconia such that it accounted for the lower density of the compounded structure. The otoconia were approximated by bricks with a basis length of 4μm by 4μm and a height of 6.5μm, which were oriented in the way indicated in Fig 23A. Experimentally it was found that the height of most otoconia falls into the range 3 to 7μm (Lindeman, 1969). To obtain the desired overall density of 2g/cm^3, a uniform spacing of 1μm (in all dimensions) between the otoconia (Fig 23A) was necessary. Young's modulus of the otoconia crystals was taken to be 104 Pa, and their Poisson's ratio 0.3. These parameters yielded otoconia which exhibit only tiny deformations.

The elastic properties of the inter-otoconial matrix directly influenced the results of our simulations, and were therefore crucial parameters. Experiments have suggested that the inter-otoconia matrix shows a much lower rigidity than the mesh layer (Lins et al., 2000). For this reason we used elasticity constants identical to that employed for the gel layer (i.e. a Young's modulus 10 Pa, and Poisson's constant 0.49). Since there is no clearly defined border between the inter-otoconial filament and the endolymph, the endolymph fluid probably fills the inter-otoconial space. Therefore we chose for the viscosity of the inter-otoconial matrix a value similar to the endolymph fluid, 0.01 Poise.

The resulting transfer functions, shown in Fig. 23, were obtained numerically for oscillations with a maximum acceleration of 1g. The filled dots indicate the amplitude and phase at the gel/mesh layer boundary in the central region of the structure, depicted in Fig. 23A. The transfer function in this zone is very similar to the corresponding result without separated otoconia (Fig. 21): Frequency independence below 5 Hz and a marked reduction of the amplitude around 10 Hz, accompanied with an increasing phase lag. The amplitude approaches zero at about 100 Hz and shows only minor deviations from this value at higher frequencies. The situation is different for the otoconia. The open dots in Fig. 23B indicate the transfer function of a single otoconia crystal from the central region of the upper layer crystals of Fig 23A. The amplitude at lower frequencies is considerably larger than at the gel/mesh layer boundary. At around 10 Hz the displacement amplitude decreases, which can be attributed to the reduced displacements of the underlying gel layer as otoconia and gel-layer move together. For frequencies around 600 Hz the otoconia undergo a resonance. Below the resonance frequency, the otoconia oscillate largely in phase with respect to the external force. Above this frequency, they move in the opposite direction. This is reflected in the change of sign of the amplitude in Fig. 23B. Depending on the magnitude of the acceleration, such a resonance could lead to considerable stresses within the inter-otoconial matrix.
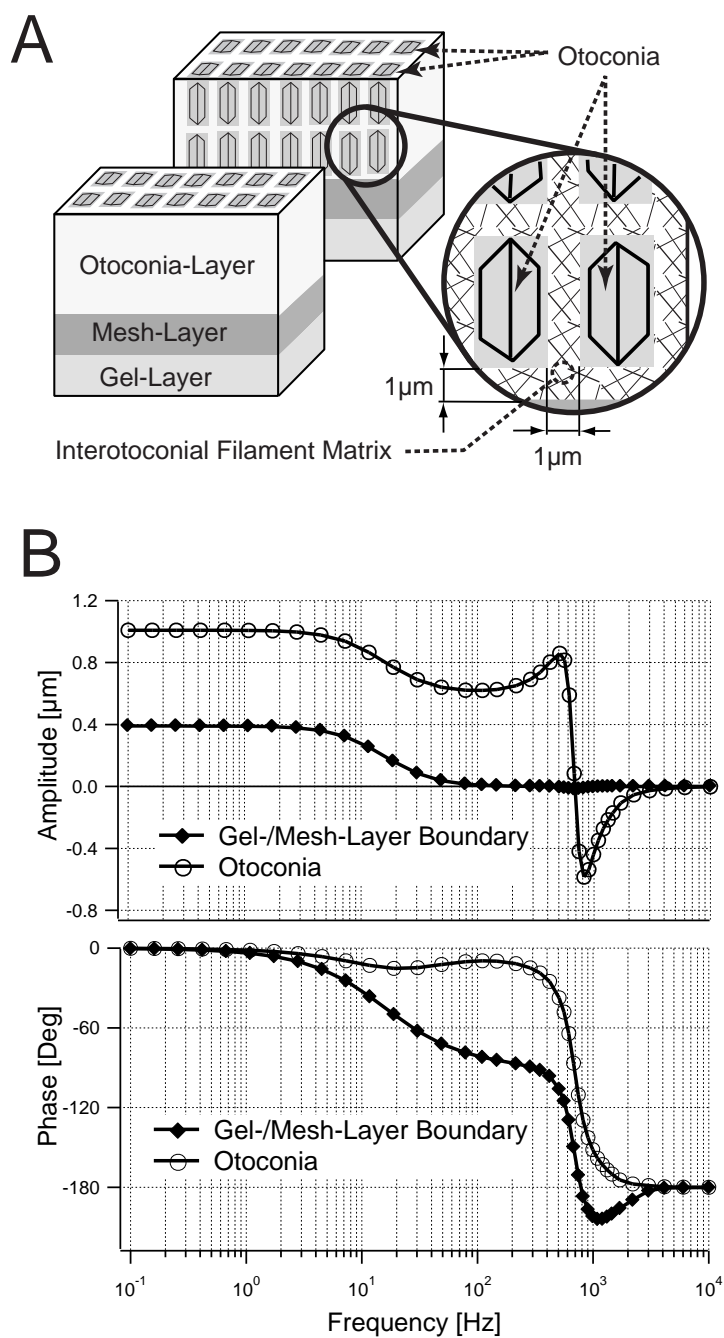
Figure 23: : Effects at higher stimulation frequencies. A) Structure of the otolith membrane. The otoconia are separated, and the space between them is filled by the "inter-otoconial matrix". B) Transfer functions for the gel/mesh layer boundary (solid dots) and otoconia (open dots). The otoconia show a resonance at about 600 Hz.

3.3.4 Discussion of the Effects at Higher Frequencies

Our results indicate that otoconia show resonant behavior within the inter-otoconial matrix. Crucial to the resonance frequency is the elasticity of the inter-otoconial matrix, E_{int}, as well as the mass of the otoconia m. Since no experimental data are available about the elasticity, our estimate relies on the observation that the rigidity of this matrix is much smaller than that of the mesh layer. On the other hand, the resonance frequency is related to these parameters by a square law:

$$f_{Res} \propto \sqrt{\frac{E_{int}}{m}}$$

This ensures that even if the elasticity is wrong by a factor of 10, the resonance frequency will only shift by a factor of 3. We estimate that the resonance frequency falls into the range between 100 Hz and 1 kHz. Even if the elasticity is similar in all parts of the otoconial layer, it is well known that otoconia have considerably different masses: otoconia from the extra-striola region are larger than those from the striola. For this reason no single resonance frequency can be expected. Instead it is more likely that a whole band of resonance frequencies exists for the different parts of the otolith membrane. We also observed small displacement amplitudes at the gel/mesh layer boundary in the frequency region around the resonance. Interestingly investigations have found otolith related responses in the vestibular nerve for stimulation frequencies in the range between 200 and 400 Hz (Young et al., 1977). It was further shown that intense impulse noise leads to a functional long term impairment of the otolith apparatus (Perez et al., 2002).

While the mass of the otoconia and the elasticity of the inter-otoconial matrix determine the resonance frequency, the damping provided by the fluid filled inter-otoconial matrix specifies how pronounced the resonance is. If the damping were stronger than assumed in our simulations, the amplitude of the resonance would decrease. For an over-damped system, the resonance would vanish completely. If, on the other hand, the fluid filled inter-otoconial matrix were not strong enough to provide this magnitude of damping, oscillating acceleration in this frequency range could lead to harmful results: Due to their different masses, different parts of the otoconial layer oscillate with different phase relations. This would result in large stresses within the inter-otoconial matrix, and could ultimately lead to a disruption of the structure. In the clinic, such a process may help to clarify the origin of benign paroxysmal positional vertigo (BPPV). Resonances of the otoconia may also be linked to disorientation and stranding of whales and dolphins in areas where low frequency active sonar (LFAS) has been used. The frequencies employed in this kind of sonar fall into the frequency range where otoconia resonances may be expected. While it is accepted that the high levels of sound used in these surveillance systems

significantly impair the hearing of crustaceans, our simulations suggest an additional mechanism for these observations, provided that the mechanical properties of their otolith structure is similar to other mammals. For these reasons experiments using high sound level from this frequency range (100 - 1000 Hz), accompanied by either physiological or electro-physiological observations, could clarify these speculations, and yield valuable insight into the mechanical properties of the otoliths.

4 Hair Cell Results

4.1 Hair cell Properties

Direction and magnitude of otolith membrane deflections is detected by the hair cells (Fernandez and Goldberg, 1976*b*; Shotwell et al., 1981). Short hair bundles, called stereocilia, are embedded into the gel layer (Fig. 4). They are inter-connected via tip-links (Hackney and Furness, 1995; Howard and Hudspeth, 1987), and linked to a single long hair, the kinocilium. Bending of the hair bundle due to a deformation of the gel layer leads to direction-specific hyper-polarization or depolarization of the hair cell. The direction leading to a maximum depolarization is indicated by the *polarization vector*. The polarization vectors of different hair cells are not randomly distributed over the epithelium, but show a distinct pattern (Lindeman, 1969), indicated by the arrows in Fig. 24.
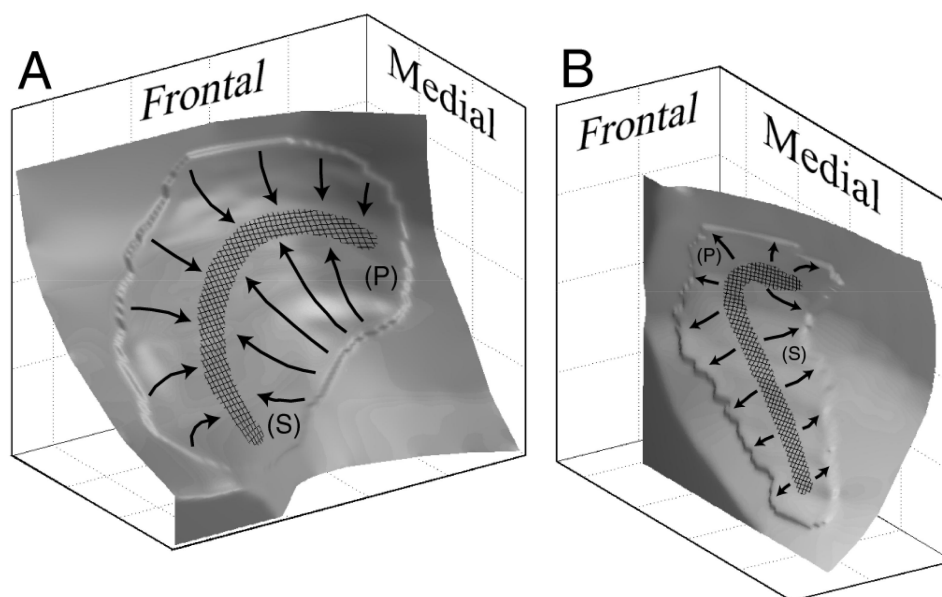
Figure 24: Hair cell polarization directions. Bending of the stereocilia in the direction indicated by the arrows leads to depolarization of the hair cells and an increase of the firing rate in corresponding vestibular fibres. The letters (S) and (P) refer to Fig. 26.

Since we are dealing with curved 3-dimensional surfaces, we needed to determine the 3D components of these polarization vectors. They were obtained by generating a two-dimensional vector-field according to the observations by Lindeman, and then projecting this field onto the curved macula. The intra-cellular hair cell potential depends on the cosine of the angle between the local polarization vector and the hair cell deflection (Shotwell et al., 1981). It was further assumed that the hair

cell potential is linearly related to the magnitude of deflection, which is probably justified as long as the external acceleration is smaller than about 3g (Fernandez and Goldberg, 1976c).

Depending on the location on the epithelium, two types of vestibular fibres can be distinguished: Tonic/phasic units, which innervate hair cells situated in the *striola* region, indicated by the shaded, band-like central region in Fig. 24, and tonic units linked to the extra-striola region (Goldberg et al., 1990b). This distinction does not coincide with the morphological type I and II hair cells: Type I cells in the striola region contribute to tonic/phasic units while similar cells in the extra-striola region are innervated by tonic units.

Tonic units show a firing rate proportional to the amount of deflection. For the investigation of dynamic stimulations, the output of tonic/phasic units are of great interest. Signals in the vestibular nerve related to these units are composed of a transient, velocity dependent part which reflects the movement of the otolith membrane due to changing acceleration, and a component that reflects the magnitude of the hair bundle bending. The origin of the regional differences of the unit properties are not clear yet. Based on morphological and theoretical considerations, Lim (Lim, 1976) and Kondrachuk (Kondrachuk, 2002) have argued that hair bundle displacements in the striola region are due to fluid flow in the gel layer. As implied by these investigations, it will be assumed that tonic/phasic properties already exit at the hair cell level.

We assumed further that bending of the kinocilium determines the movement of the stereocilia and is linearly related to the polarization of the hair cells. In extra-striola regions, the tips of the kinocilia are attached to the mesh layer (Kachar et al., 1990) or even protrude into the otoconia layer (Lim, 1976; Ross et al., 1987). In contrast, the kinocilium of hair cells in the striola seems to be shorter (Fontilla and Peterson, 2000). For these hair cells it is not clear if or where the kinocilium is actually attached to the otolith membrane. Under dynamic stimuli, the gel displacement is in general no longer a linear function of the distance to the apical surface of the hair cell: at the onset of acceleration, the upper parts of the gel layer get displaced proportionally more than parts close to the epithelium. If the tips of the kinocilia in the striola are close to the mesh layer, this would therefore result in the largest sensitivity for motion. Because of this, we assume that the direction and magnitude of the displacement at the gel/mesh layer boundary is proportional to hair cell excitation.

In summary, the deviation of the local hair cell potential (HCP) from its resting potential was calculated by

$$HCP \propto \vec{p} \cdot \vec{u} = |u|\cos(\vec{p}\,\vec{u}); \qquad |p| = 1 \tag{106}$$

where $\vec{p}$ is the normalized polarization vector, $\vec{u}$ the displacement of the otolith membrane at the border between gel and mesh-layer, and "·" indicates a scalar product. In addition to this, the transformation from a dynamic acceleration stimulus to hair cell responses in the striola region are described by the use of fractional calculus (Hess, 1992).

4.2 Hair cell responses under static conditions

4.2.1 Excitation Maps

After combining the otolith membrane displacements with the hair cell characteristics it is possible to calculate hair cell excitation at every point on the macula. This contrasts with single cell recordings, which can present only the activation of individual cells. Since the displacements vary for different acceleration magnitudes as well as directions, the resulting excitation patterns indicate different spatial representations of those accelerations.

Figure 25 shows the distribution of hair cell excitations for the upright orientation (middle), and for the head tilted 30° right- (top) or left- (bottom) ear down. To this purpose, the excitation patterns on the curved otolith surfaces were projected into the head planes, indicated by the small coordinate-system on the figure. The activation varies rather smoothly over the epithelium, with the exception of regions indicated here by dashed lines, which are approximately perpendicular to the striola. In these regions a rapid change of the polarization occurs within a range of about hundred micrometers. They can be found in the ventral part of the saccule and the medial part of the utricle. The shape and location of these regions is related to the direction of acceleration.
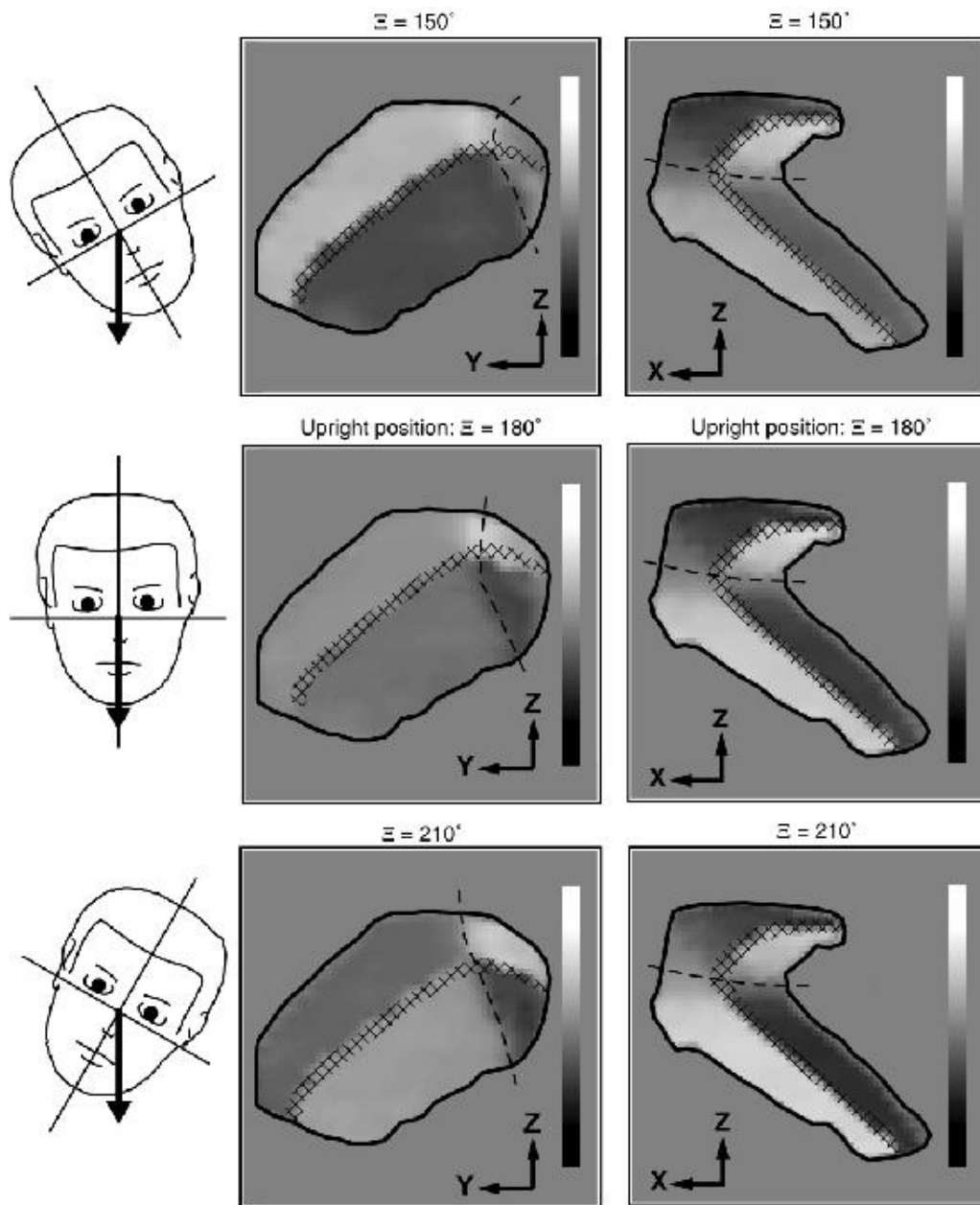
Figure 25: Excitation maps of left utricle and saccule for three directions of acceleration. The background color represents no polarization, while black and white indicate depolarization and hyper-polarization, respectively. The maps are projections on the main head planes (as indicated by the coordinate systems in Figs. 18 and 19. Shaded regions depict the location of the striola and dashed lines indicate areas where the hair cell polarization changes rapidly.

4.2.2 Response Curves

During systematic changes in roll and pitch, the polarization at different locations on the macula consisted of only a limited set of activation patterns. Figure 26 shows two such patterns for utricle and saccule. The locations of the corresponding cells are indicated in Fig. 24 by the labels "P" and "S" on the otolith surfaces.
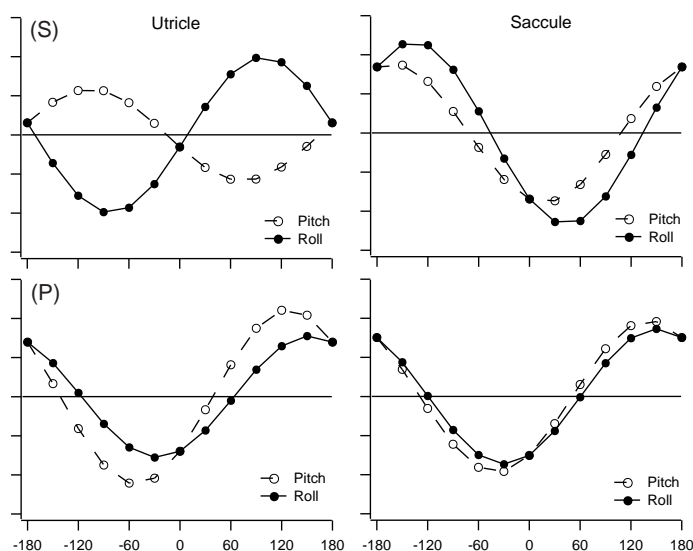

Figure 26: Examples of polarization for roll (dark points, solid line) and pitch (light points, dashed line) at the locations indicated with (S) and (P) in Fig. 24. The left column shows utricular hair cells, the right column saccular hair cells. Zero on the abscissa indicates the upright orientation, and positive angles leftward and forward tilts, respectively. The horizontal line represents zero polarization and positive values indicate hyper-polarization.

The graphs in Fig. 26 are remarkably similar to the recordings of the vestibular nerve activity during static tilt experiments (Fernandez et al., 1972). The requirement to simultaneously match amplitudes as well as phases for the roll and the pitch data imposes considerable restrictions on the orientation of the otolith macula and the directions of hair cell polarization, and eliminates the possibility to simply select the best-matching patterns for roll or pitch. Note the similarities between the P-figures of the saccule and the utricle.

4.2.3 Discussion of Static Hair cell Responses

Investigations into peripheral vestibular activity have up to now been restricted to the analysis of individual vestibular nerve signals. Our simulations present for

the first time a realistic image of the activation patterns over the whole otolith epithelium. We were surprised to find small regions, indicated by dashed lines perpendicular to the striola in Fig. 25, where the excitation level changes rapidly over a short distance. The location and shape of these regions might provide a important cue for the determination of head orientation.

Since type II cells are innervated by a single vestibular cell and the region of influence of multi-bouton type I cells is usually restricted to hair cells with a very similar on-direction (D. Dickman, private communication), we expect that our simulated excitation maps show a close correspondence to the activity in real vestibular nerve cells. If the neural connections between the otolith epithelium and the vestibular nuclei exhibit a topographic mapping, the same patterns should be found in the activity of cells in the vestibular nucleus. This is supported by the good agreement between typical activity patterns exhibited by our model during systematic changes in pitch an roll, and corresponding experimental data (Fernandez et al., 1972). Thereby we could not simply select the best-fit pattern: of all possible combinations of amplitude and phase shift, only a subset of all possible patterns was found in our data. We found that there are regions on the saccule and utricle where polarization patterns are rather similar (Fig. 26, "P"-curves). This stems from the fact that the local orientation of the maculae and the polarization vectors of the hair cells closely match in these regions. Contrary to the view that utricle and saccule provide complimentary information, this may indicate that small parts of them yield almost overlapping information. Utricle and saccule afferent fibers are usually distinguished experimentally under the assumption that such regions do not exist. While procedures applying this assumption are valid for most of them, our findings suggest that there may be a small number of utricle nerves that are mistaken as saccule fibers.

The interpretation of peripheral vestibular signals has so far concentrated on the transduction properties of individual neurons, or on the interaction between two spatio-temporally different neurons (Angelaki, 1992; Angelaki et al., 1992; Hess and Angelaki, 1993; Angelaki and Dickman, 2000). The emergence of distinct activation patterns for different static head orientations indicates an alternative option: the information about head acceleration could also be contained in a distributed representation over the whole epithelium. Large areas with similar innervation, as seen in Figure 25, would render such a representation more stable than the interpretation of signals from individual neurons. Since we want to understand the information transmitted to the brain by the hair cells, the knowledge about force-displacement relations of the macula is a first step to achieve this goal.

4.3 Hair cell responses under dynamic conditions

4.3.1 Spatio-Temporal Excitation Maps

Based on the displacements at the gel/mesh layer boundary, the distribution of hair cell polarization vectors, and fractional calculus we calculated the time dependent excitation of hair cells at location along the striola.
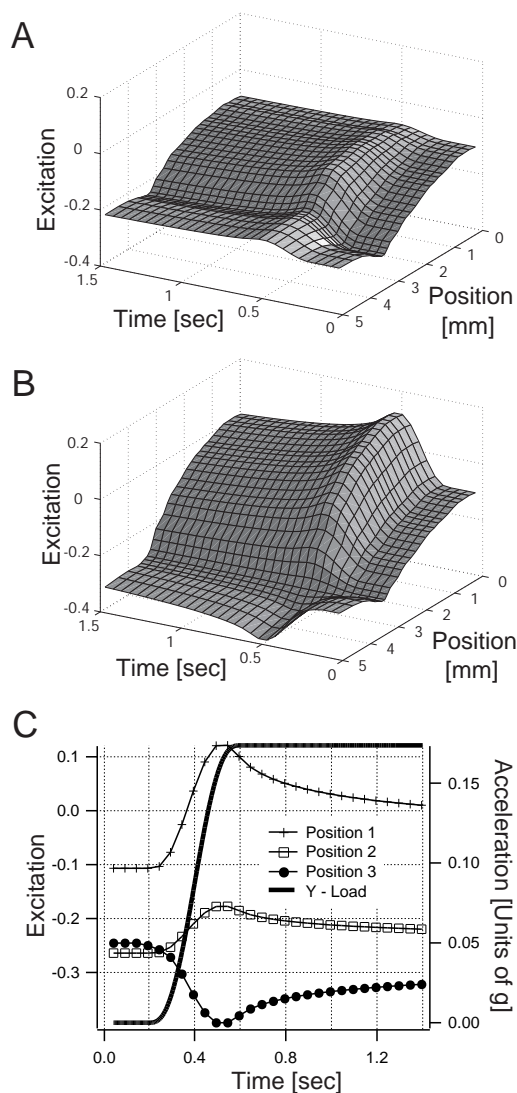

Figure 27: : Time course of utricular hair cell excitation over the striola. A and B correspond to nose down and left ear down tilts, respectively. "Position" indicates the parameterized location on the striola. The units of excitation are arbitrary. C shows the time course of excitation at various positions in A (0, 3, and 5mm), along with the acceleration along the interaural axis.

To investigate neural responses to natural stimuli, we chose small head tilts. Starting from an upright position, the head rotated smoothly within 0.4 s forward (Fig. 27A) or to the side (left ear down, Fig. 27B). The final tilt angle was 10° with respect to head upright position. Figure 27 shows the resulting excitation of utricular striola cells. Zero on the "Position" axis corresponds to the lateral end of the left utricle, and positive values parameterize the locations along the bent striola. At the beginning ("Time" equal zero) the head is in an upright position, and the excitation corresponds to the hair cell excitation in a static head-upright orientation. After 0.2 s the head tilt starts, and finishes at 0.6 s. During this time, the excitation represents the displacement as well as the displacement-velocity of the utricular structure. Excitation (or inhibition) reach their maximum value before the end of the head movement, and then approach the steady state value for the head tilted orientation. Figures 27A and B show that different tilt directions lead to clearly distinct excitation patterns. For a given tilt direction, however, the time courses at different striola positions are quite similar. Fig. 27C presents the excitation at three positions along the striola for the left ear down tilt case (Fig 27B). The resulting traces correspond to sections through the surface in Fig 27B at three different positions, parallel to the time axis. For all three traces, the moment of maximum excitation is identical, and the time during which the maximum excitation decays to the tonic state is similar. Figure 27C also shows the magnitude of gravitational acceleration along the interaural axis (thick, solid line).

4.3.2 Coding of Tilt Direction

The patterns of maximum excitation due to tilts into various directions are summarized in Fig. 28 for both otoliths. Here the parameterization of the utricle striola is identical to the one chosen in Fig. 27, while for the saccule zero corresponds to the ventral end of the striola. For the thin solid line in the third row, left column, the curves correspond to a section through the surface in Fig 27B (left ear down) at the time of maximum excitation (ca. 0.5 s), parallel to the "Position" axis. The tilt direction is characterized by an angle: 0° corresponds to forward tilt, 90° to left ear down tilt, 180° to backward tilt, and so on. Excitations that correspond to movements into opposite directions are grouped in the sub-figures. Maximum excitations at smaller angles (0°, 45°,...) are indicated by thin lines, while the corresponding larger angles (180°, 225°,...) are indicated with thick lines. The dashed lines indicate the starting, tonic excitation in a head upright position.

Though maximum excitations into opposite directions can look very different, they closely represent mirror images of each other with respect to the initial excitation: The "excitation difference", defined as the area between the initial excitation curve and the excitation curve in the tilted orientation, is similar at all positions on the

striola. For a head tilt left-ear-down, the excitation difference is indicated by the shaded area in Fig 28. Interestingly, the functional shape of the excitation curve does not change strictly proportional to the tilt direction. There are contrary successive tilt angles where the changes are large (0° to 45° at the utricle) and other angles where they are small (45° to 90°). Though it might be expected that this kind of acceleration stimulus predominantly leads to utricle responses, we also found substantial excitations at the saccule.
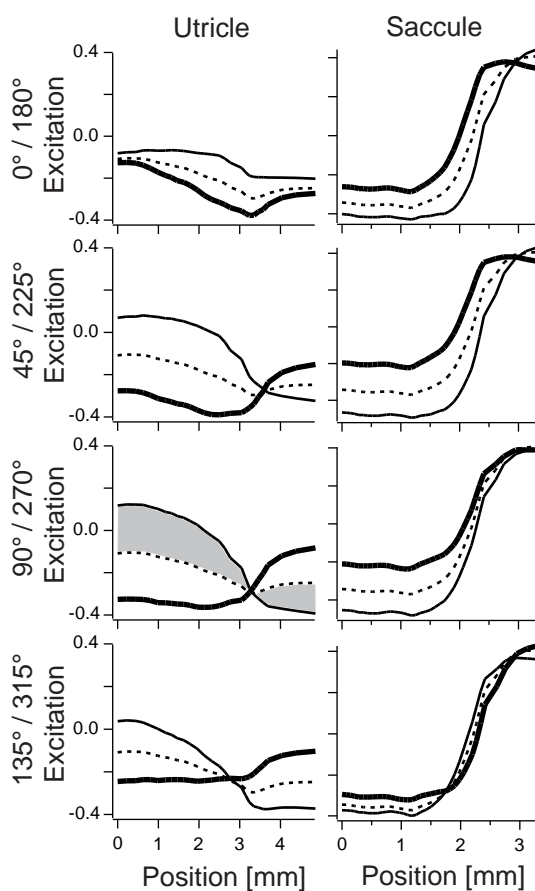
Figure 28: : Maximum excitation for tilts into different directions, indicated by the angles: 0° corresponds to nose down, 90° to left ear down tilt etc . The excitations are shown with respect to their position on the striola. Tilts into opposite directions are grouped in the sub-plots: The thin line indicates the excitation due to low-angle tilts, while the thick line corresponds to large angles. Along with the maximum excitation, the initial state, corresponding to head upright position is included (dashed lines).

4.3.3 Discussion of Dynamic Hair cell Responses

One goal of our study was to understand the neural representation of head movements. The neural activity in the vestibular nerve is a product of mechanical displacements, inter- and intracellular signal processing. Therefore a complete understanding of the system requires knowledge about the mechanical displacement of the otolith membrane. We have restricted our presentation to the immediate effects of displacements on hair cell excitation, since the implications of otolith-otolith and otolith-canal convergence are still under investigation. Velocity sensitive hair cells are chiefly found in the narrow striola region of the otoliths. This allowed us to characterize these cells with a single position parameter, i.e. by their location along the striola.

In Figs. 27A and B, the time course of excitation over the whole striola is shown for different directions of head tilts. Since responses to sensory inputs are most likely optimized for natural, everyday movements, we used natural small, 10° head tilts in this study. We found that the excitation patterns which arise from nose down and left ear down tilts are substantially different. This may indicate that the direction of head acceleration and changes of the acceleration are coded in a spatially distributed excitation pattern. It can further be noted that although both excitation patterns are due to 10° tilts, left ear down tilts seem to be more effective, since the amplitudes are larger in Fig. 27B.

Figure 27C shows that dynamic excitation responses are a mixture of tonic and phasic components. Peak excitations occur simultaneously on different locations of the striola. This indicates that the mechanical properties of the otolith structure induce no time delays in the displacement between different parts of the striola, and no information on tilt direction is coded here. Also the temporal decay of the excitation patterns yields no information on the tilt direction: As Fig. 27C shows, the time course of the decay from the maximum to the tonic state is similar throughout the striola. Both observations support the assumption that tilt direction is coded as spatially distributed activation pattern.

To test this assumption more systematically, maximum excitations were calculated for several tilt directions of the head (Fig. 28). They were chosen because the maximum excitation, together with the knowledge about the initial state, can be taken as a suitable representation of the phasic part of the excitation. Several conclusions can be drawn from Fig. 28. While it is generally assumed that the saccule is unimportant for detecting movements around the head upright position, our calculations indicate that in dynamic situations this might be wrong. Though the largest excitation change from the initial to the maximum state is generally smaller for the saccule, it is still a large fraction of the corresponding value for the utricle. In addition, the contribution of the two otoliths to a central estimation of

head movement may be influenced by the overall excitations change from all parts of the striola. In Figure 28, this is indicated by the gray area for head tilts to the left. The sub-plots "0°/180°" in the same figure suggest that the saccule may be just as important as the utricle in the detection of head movements. One further observation drawn from Fig. 28 concerns the sensitivity regarding the detection of head movement directions. The maximum excitations for tilts into the 45°/225° and 90°/270° directions are very similar for the utricle as well as the saccule. On the other hand these two sets are rather different than the other sets: Nose down tilts may be clearly distinguished from left ear down tilts. This indicates that otoliths show direction-depending sensitivities for the detection of head tilt direction. One way to improve this situation would be to use information from the left and right ear in the formation of a differential neural signal. Such a process has been proposed by Green (Green and Galiana, 1998).

5   Conclusions

Studies of the otolith system try to understand which information about the orientation and movement of the head is transduced by them, the way this information is represented in the brain and how it is integrated with sensory cues from other systems. The results presented in this investigation show that numerical simulation of otolith membrane mechanics can yield valuable insight into acceleration processing of this apparatus. It has been demonstrated that the model is able to reproduce measurements from the vestibular nerve. This indicates that 3D models of the otolith membrane provide a way to determine all the information available to the brain. In contrast recordings from the vestibular nerve can only measure small samples of it.

Still much work is needed for a comprehensive understanding of the otoliths and the vestibular system in general. Experimental investigations are particulary important. Regarding the otolith membrane, experiments like those performed by Benser et al. (Benser et al., 1993) would be very helpful: After removal of the otoconia layer markers were placed on the mesh layer, and their displacement was then used to determine material properties of the membrane. Since these experiments employed the frog sacculus, similar investigations are needed for mammal otoliths. A thorough understanding of otolith membrane mechanics also requires measurement of elasticity of the inter-otoconial matrix. Up to now only a qualitative result is available (Lins et al., 2000). This and additional physiological testing could clarify if the proposed resonance within the otoconia layer exists, as predicted by our simulations.

It is well known that different parts of the otolith membrane exhibit different morphological properties. Most notably in this regard are differences between the striola and the extra-striola region (Lim, 1976). These differences are probably also reflected in altered mechanical parameters. A marked improvement of our model could be obtained by including these differences. Regional differences exist not only with respect to the otolith membrane. Hair cells (Fontilla and Peterson, 2000) and the interconnections between them (Fernandez et al., 1990) are also affected. Experimental investigations are needed to clarify the localization and purpose of these differences.

All these suggestions call for a verification of the results obtained so far. This should build a reliable basis for subsequent investigations concerning otolith related information processing by the brain. Comparison of numerically obtained results with certain experimental findings could then be used to determine the limits of this model. Two types of experimental findings come to mind: Recordings from the vestibular nerve and subsequent stages of information processing could be helpful to determine the properties of the interaction between hair cells and vestibular nerves. Psycho-physical experiments might further yield important clues. It has been argued that the perception of head tilt is determined by otolith responses (Dai et al.,

1989). Related experiments usually measure the subjectively perceived amount of tilt for different angles in the roll axis. The findings indicate that humans systematically mis-perceive tilt magnitude. Perception data are available for tilts that cover all tilt directions. These data sets indicate that humans not only make systematic errors but also exhibit tilt-depending sensitivities in the perception of 3D body orientations. Similarly the numerical model of the otoliths indicates higher or lower sensitivity to changes about certain head positions. A link between psychophysical and numerically obtained results would support the validity of the model. It is further interesting since psycho-physical findings usually involve many steps of information processing. Evidence of direct involvement of a sensory system in generating a certain perception thus helps to clarify the functional significance of the sensor.

References

Angelaki, D. (1992), 'Spatio-temporal convergence (stc) in otolith neurons.', *Biol Cybern* **67**(1), 83–96. 4.2.3

Angelaki, D. and Dickman, J. (2000), 'Spatiotemporal processing of linear acceleration: Primary afferent and central vestibular neuron responses.', *J Neurophysiol* **84**(4), 2113–2132. 4.2.3

Angelaki, D., Perachio, A., Mustari, M. and Strunk, C. (1992), 'Role of irregular otolith afferents in the steady-state nystagmus during off-vertical axis rotation.', *J Neurophysiol* **68**(5), 1895–1900. 4.2.3

Assad, J., Shepherd, G. and Corey, D. (1991), 'Tip-link integrity and mechanical transduction in vertebrate hair cells.', *Neuron* **7**, 985–994. 1.3

Bathe, K. and Wilson, E. (1976), *Numerical methods in finite element analysis.*, Prentice-Hall Inc, Englewood Cliffs. 2.2

Benser, M., Issa, N. and Hudspeth, A. (1993), 'Hair-bundle stiffness dominates the elastic reactance to otolithic-membrane shear.', *Hear Res* **68**(2), 243–252. 1.2, 3.1, 3.2.5, 5

Blanks, R., Curthoys, I. and Markham, C. (1975), 'Planar relationship of the semicircular canals in man.', *Acta Otolaryngol* **80**(3-4), 185–196. 1.2

Curthoys, I., Betts, G., Burgess, A., MacDougall, H., Cartwright, A. and Halmagyi, G. (1999), 'The planes of the utricular and saccular maculae of the guinea pig.', *Ann NY Acad Sci* **871**, 27–34. 1.1, 1.2

Dai, M., Curthoys, I. and Halmagyi, G. (1989), 'A model of otolith stimulation.', *Biol Cybern* **60**(3), 185–194. 3.2.5, 5

Damiano, E. and Rabbitt, R. (1996), 'A singular perturbation model of fluid dynamics in the vestibular semicircular canal and ampulla.', *J Fluid Mech* **307**, 333–372. 1.1

Diamond, S. and Markham, C. (1992), 'Validating the hypothesis of otolith asymmetry as a cause of space motion sickness.', *Ann N Y Acad Sci* **656**, 725–731. 1.1

Fernandez, C. and Goldberg, J. (1976*a*), 'Physiology of peripheral neurons innervating otolith organs of the squirrel monkey. i. response to static tilts and to long-duration centrifugal force.', *J Neurophysiol* **39**(5), 970–984. 1.1

Fernandez, C. and Goldberg, J. (1976b), 'Physiology of peripheral neurons innervating otolith organs of the squirrel monkey. ii. directional selectivity and force-response relations.', *J Neurophysiol* **39**(5), 985–995.   1.1, 4.1

Fernandez, C. and Goldberg, J. (1976c), 'Physiology of peripheral neurons innervating otolith organs of the squirrel monkey. iii. response dynamics.', *J Neurophysiol* **39**(5), 996–1008.   4.1

Fernandez, C., Goldberg, J. and Abend, W. (1972), 'Response to static tilts of peripheral neurons innervating otolith organs of the squirrel monkey.', *J Neurophysiol* **35**(6), 978–997.   1.1, 4.2.2, 4.2.3

Fernandez, C., Goldberg, J. and Baird, R. (1990), 'The vestibular nerve of the chinchilla. iii. peripheral innervation patterns in the utricular macula.', *J Neurophysiol* **63**(4), 767–780.   1.3, 5

Flock, A. (1964), 'Structure of the macula utriculi with special reference to directional interplay of sensory responses as revealed by morphological polarization.', *J Cell Biol* **22**, 413–431.   3.3.2

Fontilla, M. and Peterson, E. (2000), 'Kinocilia heights on utricular hair cells.', *Hear Res* **145**(1-2), 8–16.   4.1, 5

Glasauer, S. and Merfeld, D. (1997), Modeling three-dimensional vestibular responses during complex motion stimulation., *in* 'Three-dimensional kinematics of eye, head and limb movements', Harwood academic publishers.   3.2.5

Goldberg, J., Desmadryl, G., Baird, R. and Fernandez, C. (1990a), 'The vestibular nerve of the chinchilla. iv. discharge properties of utricular afferents.', *J Neurophysiol* **63**, 781–790.   1.1, 3.1

Goldberg, J., Desmadryl, G., Baird, R. and Fernandez, C. (1990b), 'The vestibular nerve of the chinchilla. v. relation between afferent discharge properties and peripheral innervation patterns in the utricular macula.', *J Neurophysiol* **63**, 791–804.   1.2, 1.3, 4.1

Goldberg, J. and Fernandez, C. (1971), 'Physiology of peripheral neurons innervating semicircular canals of the squirrel monkey. i. resting discharge and response to constant angular accelerations.', *J Neurophysiol* **34**(4), 635–660.   1.3

Grant, J. and Best, W. (1986), 'Mechanics of the otolith organ - dynamic response.', *Ann Biomed Eng* **14**(3), 241–256.   1.2, 3.2.5

Grant, J. and Best, W. (1987), 'Otolith-organ mechanics: Lumped parameter model and dynamic response.', *Aviat Space Environ Med* **58**, 970–976.   1.2, 3.2.5

Grant, J., Best, W. and LoNigro, R. (1984), 'Governing equations of motion for the otolith organs and their response to a step change in velocity of the skull.', *J Biomed Eng* **106**(4), 302–308. 1.2, 3.2.5

Grant, J. and Cotton, J. (1990), 'A model for otolith dynamic response with a viscoelastic gel layer.', *J Vestib Res* **1**(2), 139–151. 1.2, 3.1, 3.2.4, 3.2.5, 3.3.2

Grant, J., Huang, C. and Cotton, J. (1993), 'Theoretical mechanical frequency response of the otolithic organs.', *J Vestib Res* **4**(2), 137–151. 1.2, 2.3, 3.1, 3.2.5, 3.3.2

Green, A. and Galiana, H. (1998), 'Hypothesis for shared central processing of canal and otolith signals.', *J Neurophysiol* **80**(4), 2222–2228. 4.3.3

Hackney, C. and Furness, D. (1995), 'Mechanotransduction in vertebrate hair cells: structure and function of the stereociliary bundel.', *Amer J Physiol-Cell Physiol* **37**, C1–C13. 4.1

Haslwanter, T., Jaeger, R., Mayr, S. and Fetter, M. (2000), 'Otolith-canal interaction during off-vertical axis rotations.', *Exp Brain Res* **134**, 96–106. 3.2.5

Hess, B. (1992), 'Three-dimensional head angular velocity detection from otolith afferent signals.', *Biol Cybern* **67**(4), 323–333. 2.4, 4.1

Hess, B. and Angelaki, D. (1993), 'Modelling spatiotemporal properties of directionally sensitive multi-input single-output systems.', *Biol Cybern* **69**, 407–414. 4.2.3

Howard, J. and Hudspeth, A. (1987), 'Mechanical relaxation of the hair bundle mediates adaptation in mechanoelectrical transduction by the bullfrog's saccular hair cell.', *Proc Natl Acad Sci* **84**, 3064–3068. 4.1

Hudetz, W. (1973), 'A computer simulation of the otolith membrane.', *Comput Biol Med* **3**, 355–369. 3.2.5

Jaeger, R., Takagi, A. and Haslwanter, T. (2002), 'Modeling the relation between head orientations and otolith responses in humans.', *Hear Res* **173**, 29–42. 3.3.1, 3.3.2

Kachar, B., Parakkal, M. and Fex, J. (1990), 'Structural basis for mechanical transduction in the frog vestibular sensory apparatus: I. the otolithic membrane.', *Hear Res* **45**, 179–190. 1.2, 5, 7, 1.3, 3.2.5, 3.3.2, 4.1

Kondrachuk, A. (2000), 'Computer simulation of the mechanical stimulation of the saccular membrane of bullfrog.', *Hear Res* **143**(1-2), 130–138. 1.2, 3.1, 3.2.4, 3.2.5

Kondrachuk, A. (2001*a*), 'Finite element modeling of the 3d otolith structure.', *J Vestib Res* **11**(1), 13–32. 3.1

Kondrachuk, A. (2001*b*), 'Models of the dynamics of otolithic membrane and hair cell bundle mechanics.', *J Vestib Res* **11**(1), 33–42. 3.3.2

Kondrachuk, A. (2002), 'Models of otolithic membrane-hair bundle interaction.', *Hear Res* **166**(1-2), 96–112. 4.1

Kondrachuk, A. and Sirenko, S. (1987), 'A two-dimensional statistical model of the otolith.', *Kosm Biol Aviakosm Med* **21**(6), 70–76. Russian. 1.1

Lai, W., Rubin, D. and Krempl, E. (1993), *Continuum mechanics.*, Pergamon Press, Oxford. 2.1

Leigh, R. and Zee, D. (1999), *The neurology of eye movements.*, Oxford University Press, New York. 1.1

Lim, D. (1976), 'Morphological and physiological correlates in cochlear and vestibular sensory epithelia.', *Scanning Electron Microscopy* **2**, 270–275. 1.2, 1.3, 4.1, 5

Lindeman, H. (1969), 'Studies on the morphology of the sensory regions of the vestibular apparatus.', *Ergeb Anat Entwicklungsgesch* **42**, 1–113. 1.2, 1.2, 1.2, 3.3.3, 4.1

Lins, U., Farina, M., Kurc, M., Riordan, G., Thalmann, R., Thalmann, I. and Kachar, B. (2000), 'The otoconia of the guinea pig utricle: Internal structure, surface exposure, and interactions with the filament matrix.', *J Struct Biol* **131**(1), 67–78. 1.2, 6, 3.3.3, 5

Markham, C., Diamond, S. and Stoller, D. (2000), 'Parabolic flight reveals independent binocular control of otolith- induced eye torsion.', *Arch Ital Biol* **138**(1), 73–86. 1.1

Merfeld, D., Young, L., Oman, C. and Shelhamer, M. (1993), 'A multidimensional model of the effect of gravity on the spatial orientation of the monkey.', *J Vestib Res* **3**(2), 141–161. 3.2.5

Mittelstaedt, H. (1995), 'Evidence of somatic gravicetion from new and classical investigations.', *Acta Otolaryngol Suppl* **520**(1), 186–187. 1.1

Money, K., Bonen, L., Beatty, J., Kuehn, A., Sokoloff, M. and Weaver, R. (1971), 'Physical properties of fluids and structures of vestibular apparatus of the pigeon.', *Am J Physiol* **220**, 140–147. 3.1, 3.3.3

Oldham, K. and Spanier, J. (1974), *The fractional calculus.*, Academic Press, Orlando. 2.4

Perez, R., Freeman, S., Cohen, D. and Sohmer, H. (2002), 'Functional impairment of the vestibular end organ resulting from impulse noise exposure.', *Laryngoskope* **112**(6), 1110–1114. 3.3.4

Peters, R. (1969), Dynamics of the vestibular system and their relation to motion perception, spatial disorientation, and illusions., Technical Report CR-1309, NASA. 3.1

Rabbitt, R., Boyle, R. and Highstein, S. (1995), 'Mechanical indentation of the vestibular labyrinth and its relationship to head rotation in the toadfish, opsanus tau.', *J Neurophysiol* **73**, 2237–2260. 1.1

Rabbitt, R., Boyle, R. and Highstein, S. (1999), 'Influence of surgical plugging on horizontal semicircular canal mechanics and afferent response dynamics.', *J Neurophysiol* **82**, 1033–1053. 1.1

Rao, S. (1982), *The finite element method in engineering.*, Pergamon Press, Oxford. 2.2

Ross, M., Komorowski, T., Donovan, K. and Pote, K. (1987), 'The suprastructure of the saccular macula.', *Acta Otolaryngol* **103**, 56–63. 1.3, 4.1

Sato, H., Sando, I. and Takahashi, H. (1992), 'Computer-aided three-dimensional measurement of the human vestibular apparatus.', *Head Neck Surg* **107**(3), 405–409. 1.1, 1.2, 3.3.2

Sellick, P., Patuzzi, R. and Johnstone, B. (1982), 'Measurement of basilar membrane motion in the guinea pig using the mössbauer techique.', *J Acoust Soc Am* **72**, 131–141. 3.1

Shotwell, S., Jacobs, R. and Hudspeth, A. (1981), 'Directional sensitivity of individual vertebrate hair cells to controlled deflection of their hair bundles.', *Ann NY Acad Sci* **374**, 1–10. 1.3, 4.1, 4.1

Steer, R. (1967), The influence of angular and linear acceleration and thermal stimulation on the human semicircular canal., Sc. d. thesis, Massachusetts Institute of Technology. 3.1

Takagi, A. and Sando, I. (1988), 'Computer-aided three-dimensional reconstruction and measurement of the vestibular end-organs.', *Otolaryngol Head Neck Surg* **98**(3), 195–202. 1.1, 1.2, 3.3.2

Trincker, D. (1962), 'Transformation of mechanical stimulus into nervous excitation.', *Soc Exp Biol Symp* **16**, 289–316. 3.1, 3.3.3

Twizell, E. and Curran, D. (1977), 'A finite element model of the otolith membrane.', *Comput Biol Med* **7**(2), 131–141. 3.2.5

Viirre, E. and Demer, J. (1997), Head and eye in three dimensions during standing, walking and running., *in* 'Three-dimensional kinematics of eye, head and limb movements', Harwood academic publishers. 3.3.1

Young, E., Fernandez, C. and Goldberg, J. (1977), 'Responses of squirrel monkey vestibular neurons to audio-frequency sound and head vibration.', *Acta Otolaryngol* **84**(5-6), 352–360. 3.3.4

A   Curriculum Vitae

Name: Rudi Jaeger
Born: 03.08.1965
Place of birth: Ellwangen/Jagst
Nationality: German
Civil-Service at Johaniter-Unfallhilfe from October 1986 till April 1988

Education

Technical Gymnasium Aalen, Germany
Graduated with honors, June 1986.

Eberhard-Karls-University, Dept. of Physics, Tübingen, Germany
Louisiana State University, Dept. of Physics, Baton Rouge, USA

Diploma in Physics, April 1997, Tübingen
Diploma-thesis at the Dept. of Applied Geology entitled:
   Modellierung nichtlinearer Intrapartikelsorption in
   heterogenem Aquifermaterial.

Work Experience

Mathematical Tutor at the Dept. of Applied Geology
March 1996 - August 1996

Scientific assistant at the University Hospital Tübingen
February 1997 - November 1999

Publications

1. Haslwanter T, Jaeger R, Fetter M, Mayr S (1998) Multisensory processing during off-vertical axis rotations. Exp. Brain. Res.

2. Jaeger R, Liedl R (1999) Prognose der Sorptionskinetik organischer Schadstoffe in heterogenem Aquifermaterial. Grundwasser

3. Haslwanter T, Jaeger R, Fetter M (1999) Otolith-canal Interaction During Pitch While Rotating. New York Acad. Sci.

4. Jaeger R, Takagi A, Haslwanter T (2002) Modeling the relation between head orientations and otolith responses in humans. Hear. Res.

B   Acknowledgements

First and foremost, I like to thank Dr. Thomas Haslwanter, whose continuous encouragement and advice made this work possible. I further like to thank Professor Dr. Hanns Ruder, who greatly supported this investigation.

I am grateful to Professor Dr. Michael Fetter, Professor Dr. Peter Thier, and Professor Dr. Johannes Dichgans, who helped to realize this project.

Dr. Alexander Kondrachuk supported this investigation with ideas and critique. I especially like to thank Professor Dr. Wallace Grant for drawing my attention to the possibility of resonances in the otolith membrane.

I like to thank Dr. Helmut Mutschler and Dr. Karl Beykirch for their help and fruitful discussions.

I especially like to thank Sabine Rauscher for her patience and encouragement.